Flow Effects on Melt Structure and Entanglement Network of Linear Polymers: Results from a Nonequilibrium Molecular Dynamics Simulation Study of a Polyethylene Melt in Steady Shear

3 AUTHORS, INCLUDING:

Martin Kröger
ETH Zurich

239 PUBLICATIONS **3,828** CITATIONS

Macromolecules
ARTICLE

Flow Effects on Melt Structure and Entanglement Network of Linear Polymers: Results from a Nonequilibrium Molecular Dynamics Simulation Study of a Polyethylene Melt in Steady Shear

Chunggi Baig,*,[†] Vlasis G. Mavrantzas,[†] and Martin Kröger[‡]

[†]*Department of Chemical Engineering, University of Patras & FORTH-ICE/HT, Patras, GR 26504, Greece, and* [‡]*Polymer Physics, ETH Zürich, Department of Materials, Wolfgang-Pauli-Strasse 10, CH-8093 Zürich, Switzerland*

ABSTRACT: We present detailed results about the structural, conformational, rheo-optical, and topological properties of an entangled of $C_{400}H_{802}$ linear polyethylene (PE) melt over a wide range of shear rates (covering both the linear and the highly nonlinear viscoelastic regimes) from direct nonequilibrium molecular dynamics (NEMD) simulations of a large system containing 192 chains (corresponding to 79200 interacting atomistic units). We discuss results for (i) the probability distribution of the mean-square chain end-to-end distance and its radius of gyration, (ii) the conformation tensor, (iii) the material functions in steady shear (viscosity, normal stress differences, nonequilibrium shear compliance, hydrostatic pressure), (iv) the flow birefringence, (v) the orientation angle and order parameter, (vi) the interaction energies and their relative importance, (vii) the intermolecular pair distribution function, and (viii) the intrinsic molecular shape of the chains (represented by the isosurface plots in terms of their monomer number density), all as a function of flow strength. A detailed primitive path (PP) analysis has allowed us to examine how the flow field alters the statistical properties of the underlying topological network of the melt (probability distribution functions and mean values of PP contour length, of the number and size of entanglement strands, etc.). Our results reveal significant distortions of all these distributions due to applied flow. One of the most important results of our work is that as the shear rate is increased, the average value of the contour length goes through a maximum and the number of entanglements per chain exhibits a *shear-thinning* behavior which bears many similarities with the corresponding behavior of the shear viscosity. Overall, most of the computed rheological properties of the $C_{400}H_{802}$ melt change in a nonlinear way with the applied shear rate due to the simultaneous effect of (a) chain orientation and stretching, (b) chain rotation and tumbling under shear, and (c) chain disentanglement.

1. Introduction

It is well-known today that the complicated flow behavior of polymeric liquids has its origin in the wide spectrum of time and length scales characterizing molecular motion and structure in these systems.[1] A fundamental understanding of the relaxation mechanisms and phenomena occurring across these scales is thus a prerequisite for predicting the response of these systems to an applied flow field, both in the linear and nonlinear regimes. The situation becomes more intricate by the fact that this tremendous multiplicity of time and length scales depends in a rather complicated way on a number of parameters, such as chemical constitution, chain length, molecular architecture, thermodynamic conditions (temperature, density, pressure), type and strength of external field, nature of surrounding molecules (environment), and many others.[1–4] Focusing, in particular, on the rheological properties of a homopolymer melt at prespecified temperature and pressure (or density) conditions, the key parameters governing viscoelasticity are chain length, molecular architecture, and type and strength of applied flow.[5–7] This explains why a large number of theoretical and experimental works today aim at understanding the role of these parameters on the structural, rheological, and flow-induced topological properties of a polymer melt. The long-term goal is to build on this understanding in order to establish links between different levels in the system description in a systematic and consistent way through appropriate "coarse-graining" of atomistically detailed representations of the polymer sample.

Flow can induce a variety of phenomena unique to polymeric or macromolecular liquids such as phase transitions,[8] strain hardening,[2,4,9–12] replication,[13,14] crystallization,[15–22] and increase in the melting point.[18,22,23] Despite significant advances in the development of experimental techniques over the years,[18,20,24–26] an explanation of these phenomena in terms of the microscopic processes accompanying the application of the flow (by directly probing, for example, molecular motion on pico- or microsecond time scales) is still out of reach. In this direction, direct nonequilibrium molecular dynamics (NEMD) simulations offer a promising avenue since they allow one to track dynamics over a window of time scales (from times corresponding to the motion of individual monomers to times corresponding to the dynamics of entire chains).[27] Thus, it is not surprising that a lot of effort has been put in the last decades in the development of rigorous NEMD algorithms guided from principles of nonequilibrium statistical mechanics[27–29] and of appropriate boundary conditions for systems subjected to elongation[30,31] and shear[27,32] consistent with those encountered in the real experiment. We can mention, for example, the SLLOD algorithm[27] and its generalized version, the *p*-SLLOD method,[28,29] for simulating general homogeneous flows for which suitable steady-state boundary conditions exist: these are the Lees–Edwards ones for shear[33] and the Kraynik–Reinelt ones for planar elongation.[34,35] [Unfortunately, analogous boundary conditions for simulating uniaxial or biaxial elongational flows have not been formulated as yet, although for moderate flow rates the so-called beyond equilibrium molecular dynamics[36,37] (a NEMD method without boundary conditions) has been introduced as a general method for simulating arbitrary homogeneous flows.]

*Author to whom correspondence should be addressed. E-mail: cbaig@iceht.forth.gr. Telephone: +30-2610-965219. Fax: +30-2610-965223.

Atomistic NEMD studies of polymeric liquids[27,30−32,35,38] have been restricted in their majority to rather short-chain systems; this is due to some inherent difficulties associated with these very detailed simulations, namely the use of a very small MD time step (e.g., ~2 fs[39]) as compared to the longest relaxation time of the polymer which increases dramatically with chain length. As a result, very little information is available today on the dynamics of entangled polymer melts subjected to flow from direct NEMD simulations. Given that polymer chains cannot cross each other, dynamics in entangled polymers differs substantially compared to unentangled systems due to the existence of topological interactions dominating not only their diffusive behavior but also their response to an applied flow.[37,40−50] In general, even the characteristic time scales exhibited by the same long chains in response to an applied flow field can be very different when these are studied in melt than when they are considered in a dilute or in a semidilute solution.[1,7]

In the context of the tube model, chain dynamics in entangled linear polymer melts is satisfactorily described by the reptation theory of de Gennes[51] and Doi−Edwards:[52] topological constraints (entanglements) with surrounding chains restrict the motion of the chain in the region around a curvilinear tube whose main axis coincides with the axis of the chain primitive path (PP), namely the shortest path connecting the two ends of the chain and having the same topology with the chain itself relative to the constraints.[53] The tube model has been extended today to describe chain dynamics in more complex polymer systems such as branched polymers and stars.[4] In the tube model, a measure of the strength of topological interactions is provided by the value of the tube diameter, which in turn encompasses information about the density of entanglements and the average contour length of the PP. Clearly, from the perspective of the tube model, dynamics in entangled polymers can be understood by focusing on the large-scale chain conformational properties (i.e., by neglecting dynamics at the level of a few monomeric units) as expressed by the concept of the PP and as promoted by reptation, namely a one-dimensional diffusive motion in the curvilinear space of the effective tube confining lateral motion. Devising then a computational methodology that, given a configuration of the polymeric sample, could reveal the underlying entanglement network has been recognized as an issue of paramount importance in the field.[7]

A major achievement in this direction has been made by Everaers et al.,[54] who succeeded in generating the PP network for an ensemble of bead−spring chains. In their method, the system is driven to a state of minimum energy through an annealing process in which temperature is gradually lowered to zero (in a post-MD stage) by switching off all intramolecular interactions but by maintaining the spring potentials between neighboring beads and the intermolecular interactions. The method (which leads eventually to chains that are pulled taut without crossing) is applied simultaneously for all chains in the system[55] and has been found to yield results for the plateau modulus that are in qualitative and quantitative agreement with experimentally measured data for a variety of polymeric systems.[54,56] Shortly after Everaers et al. published their method of PP analysis for FENE-type polymer chain models, two geometrical methods appeared in the literature also capable of reducing computer generated polymer models to entanglement networks: (a) the Z-code (by one of us[57]) and (b) the CReTA algorithm (by Tzoumanekas−Theodorou[58]). The new methods drive the system to a state that corresponds to the minimum of the total length for all PPs in the system (as opposed to the minimum of the total energy) using a geometrical scheme for the contour-length reduction problem which is computationally more efficient than the annealing method by several orders of magnitude.[59,60] Despite differences in their specific implementation, the three methods are reported to yield similar results for the average properties of the PP network (although some quantitative discrepancy has been observed in the predictions of the annealing and the geometrical methods for the average PP contour length for monodisperse linear polymer melts).[59] Interested readers

are referred to the original papers[54,57−59] for more details on each of the three methods.

In the present work, we have embarked on a new project aiming at providing molecular-level information for the interplay between flow and entanglement network statistics in entangled polymeric liquids. The first step (carried out in this study) is to conduct extensive NEMD simulations of a model linear polyethylene (PE) melt, here $C_{400}H_{802}$, under shear over a wide range of shear rates (from the linear to the highly nonlinear regime) in order to obtain information on the effect of flow on a number of characteristic structural (e.g., chain end-to-end distance, chain radius of gyration, order parameter), viscoelastic (e.g., viscosity, normal stress coefficients, hydrostatic pressure), and topological (the PP contour length, the number of entanglements or topological constraints, the size of entanglement strands) properties. These results will be indicative of the degree to which flow affects melt structure and topology at two different levels: atomistic and mesoscopic. A second step (to be taken in a future study) will address a more conceptual problem: how one can interface the findings of this first (atomistic simulation and PP analysis) step with modern tube models under nonequilibrium conditions. Two important issues to be addressed there include flow effects on the lifetime of entanglements and the elucidation of mechanisms (such as convective constraint release) invoked by modern tube theories to describe flow phenomena deeply in the nonlinear regime.

The main body of this paper is organized as follows: In section 2, we describe in detail the atomistic system and the molecular model employed in the NEMD simulations. We also discuss briefly the basic features of the NEMD code and of the Z1 algorithm (a successor of the Z-code used for the topological analysis).[59−62] The results for the structural, viscoelastic, and topological properties of the simulated system as a function of the imposed shear rate are presented and fully discussed in section 3. We close with section 4 summarizing the most important findings of our work and the conclusions drawn.

2. Simulation Methods

2.1. System Studied and Molecular Model. The simulations reported in this work have been carried out with a strictly monodisperse $C_{400}H_{802}$ linear polyethylene (PE) melt system in a large rectangular box containing in total 198 $C_{400}H_{802}$ molecules, subject to periodic boundary conditions in all three dimensions (x, y, and z). The simulations were executed in the *NVT* statistical ensemble at temperature $T = 450$ K and density $\rho = 0.7640$ g/cm^3 (corresponding to a pressure $P = 1$ atm for the simulated system).[63,64] The simulation cell had dimensions (318.8 Å) × (86.96 Å) × (86.96 Å) along the x, y and z directions, respectively, showing that it was significantly enlarged in the flow (x-) direction in order to minimize system size effects especially at high shear rates where chains tend to orient along with the flow. On the basis of the results for the mean-square chain end-to-end distance $\langle R^2 \rangle$ and the mean-square chain radius of gyration $\langle R_g^2 \rangle$ of the $C_{400}H_{802}$ molecules that $\langle R^2 \rangle_{eq}^{1/2} = 89.5 \pm 1.2$ Å and $\langle R_g^2 \rangle_{eq}^{1/2} = 36.6 \pm 0.3$ Å at equilibrium and their maximum (plateau) values $\langle R^2 \rangle_{peak}^{1/2} = 254 \pm 2$ Å and $\langle R_g^2 \rangle_{peak}^{1/2} = 87.2 \pm 0.5$ Å occurring at the highest flow strength imposed in this study, the box dimension in the y and z directions is hence about 2.4 times larger than $\langle R_g^2 \rangle_{eq}^{1/2}$ and the dimension in the x-direction is about 3.7 times larger than $\langle R_g^2 \rangle_{peak}^{1/2}$. On the basis of the numerous NEMD works of polymeric materials in the literature,[12,22,31,32,37,40−42,45−48] this box dimension is believed to be sufficiently large to avoid system-size effects and give rise to statistically reliable results (our present box size containing about 80 000 united atoms of polymer melts is at least 4−5 times larger than most atomistic NEMD simulations that have been reported so far). A fully equilibrated (at all length scales) initial configuration was used in the simulations.

The simulations were performed with the Siepmann–Karaborni–Smit (SKS) united-atom potential model,[65] except for the fact that the rigid bond assumed in the original model was replaced by a flexible one with a harmonic potential and a relatively large spring constant. In the SKS model, intermolecular and intramolecular nonbonded interactions are represented by a 6–12 Lennard-Jones (LJ) potential:

$$U_{LJ}(r_{ij}) = 4\varepsilon_{ij}\left[\left(\frac{\sigma_{ij}}{r_{ij}}\right)^{12} - \left(\frac{\sigma_{ij}}{r_{ij}}\right)^{6}\right] \tag{1}$$

The LJ energy and size parameters had values equal to $\varepsilon/k_B = 47$ K and $\sigma = 3.93$ Å for CH_2 units, and equal to $\varepsilon/k_B = 114$ K and $\sigma = 3.93$ Å for CH_3 units, where k_B denotes the Boltzmann constant. Cross interactions between atomistic units i and j were specified by making use of the standard Lorentz–Berthelot mixing rules, namely $\varepsilon_{ij} = (\varepsilon_i\varepsilon_j)^{1/2}$ and $\sigma_{ij} = (\sigma_i + \sigma_j)/2$. A cutoff distance equal to $2.5\sigma_{CH_2}$ was used in the simulations. The intramolecular LJ interaction was active only between atoms that are separated by more than three bonds along the chain. As far as the bonded interactions are concerned (bond-stretching, bond-bending, and bond-torsional), these were described by the following expressions:

$$U_{str}(l) = \frac{1}{2}k_l(l - l_{eq})^2 \tag{2}$$

$$U_{ben}(\theta) = \frac{1}{2}k_\theta(\theta - \theta_{eq})^2 \tag{3}$$

and

$$U_{tor}(\phi) = \sum_{m=0}^{3} a_m(\cos\phi)^m \tag{4}$$

The following values of the corresponding parameter sets were used in the simulations: (a) bond-stretching constant: $k_l/k_B = 452,900$ K/Å^2, equilibrium bond length: $l_{eq} = 1.54$ Å, (b) bond-bending constant: $k_\theta/k_B = 62,500$ K/rad^2, equilibrium bond angle: $\theta_{eq} = 114°$, and (c) bond-torsional constants: $a_0/k_B = 1010$ K, $a_1/k_B = 2019$ K, $a_2/k_B = 136.4$ K, and $a_3/k_B = -3165$ K.

With the above parametrization of the SKS model, the longest relaxation time λ of the simulated $C_{400}H_{802}$ linear PE melt at $T = 450$ K and $\rho = 0.7640$ g/cm^3 comes out to be equal to 218 ± 10 ns, as estimated by the integral below the stretched-exponential curve describing the time autocorrelation function of the chain end-to-end unit vector.

2.2. NEMD Method. In the NEMD simulations, the p-SLLOD algorithm[28,29] was used derived on rigorous statistical-mechanics principles, alongside with appropriate boundary conditions for shear (namely the Lees–Edwards sliding-brick boundary conditions[33]). The p-SLLOD equations of motion with a Nosé–Hoover thermostat[66,67] for simulations at constant temperature so that the canonical ensemble is generated[67] have the following form:[28,30]

$$\dot{\mathbf{q}}_{ia} = \frac{\mathbf{p}_{ia}}{m_{ia}} + \mathbf{q}_{ia}\cdot\nabla\mathbf{u}$$

$$\dot{\mathbf{p}}_{ia} = \mathbf{F}_{ia} - \mathbf{p}_{ia}\cdot\nabla\mathbf{u} - m_{ia}\mathbf{q}_{ia}\cdot\nabla\mathbf{u}\cdot\nabla\mathbf{u} - \frac{p_\zeta}{Q}\mathbf{p}_{ia}$$

$$\dot{\zeta} = \frac{p_\zeta}{Q}$$

$$\dot{p}_\zeta = \sum_i\sum_a\frac{\mathbf{p}_{ia}^2}{m_{ia}} - dNk_BT \tag{5}$$

In eq 5, $\mathbf{q}_{ia}$, $\mathbf{p}_{ia}$, m_{ia}, and $\mathbf{F}_{ia}$ are the position vector, momentum vector, mass, and force vector of atom a in molecule i,

respectively, d denotes the space dimensionality, N is the total number of (united) atoms in the system, ζ and p_ζ are the coordinate- and momentum-like variables, respectively, of the Nosé–Hoover thermostat controlling the temperature of the system at the desired level, and $Q = dNk_BT\tau^2$ is the thermostat mass parameter. As far as the value of the relaxation time parameter τ is concerned, this was set equal to 0.24 ps in all simulations. In the simulations, the following form of the velocity gradient tensor was assumed:

$$\nabla\mathbf{u} = \begin{bmatrix} 0 & 0 & 0 \\ \dot{\gamma} & 0 & 0 \\ 0 & 0 & 0 \end{bmatrix} \tag{6}$$

corresponding to a simple steady shear flow. With expression 6 for $\nabla\mathbf{u}$, the p-SLLOD equations of motion are identical to those of the traditional SLLOD algorithm, since the term $m_{ia}\mathbf{q}_{ia}\cdot\nabla\mathbf{u}\cdot\nabla\mathbf{u}$ in the momentum equation, eq 5, vanishes identically.

The set of evolution equations (eq 5) were numerically integrated with the reversible reference system propagator algorithm (r-RESPA),[68] allowing for two different time scales in an MD step: a large time scale for the integration of the slowly-varying forces (corresponding to the nonbonded intermolecular and intramolecular LJ interactions, the Nosé–Hoover thermostat, and the flow field), and a small time scale for the integration of the fast-varying forces (corresponding to the bond-stretching, bond-bending, and bond-torsional interactions); see Supporting Information for details on the time integrator with the r-RESPA. In the present simulations, the large and small time steps were equal to 2.35 and 0.47 fs, respectively. A broad range of shear rates $\dot{\gamma}$ were studied corresponding to Weissenberg numbers ($Wi \equiv \lambda\dot{\gamma}$ with $\lambda = 218 \pm 10$ ns) in the interval [0.54, 20000] (corresponding to 2.48×10^6 s$^{-1} \leq \dot{\gamma} \leq 9.90 \times 10^{10}$ s^{-1}) extending from the linear to the highly nonlinear viscoelastic regime. The present study for a variety of structural and rheological properties shows that the melt system exhibits linear viscoelastic behaviors up to $Wi \approx 2$ (corresponding to $\dot{\gamma} \leq 9.2 \times 10^6$ s^{-1}) and highly nonlinear viscoelastic behaviors for $Wi \geq 500$ (corresponding to $\dot{\gamma} \geq 2.29 \times 10^9$ s^{-1}).

2.3. Topological Analysis. The reduction of an atomistic configuration to the PP network (ensemble of the shortest multiple disconnected paths) was performed using the procedure described in detail in ref 62. In this method (also known as the Z1-code[57,60]) all chain ends are held fixed in space, excluded volume interactions are disabled but chain uncrossability is retained, and a set of geometric operations is employed capable of monotonically reducing the contour lengths of all polymer chains in the system to a minimum value. The method produces eventually a PP for each chain thereby reducing the atomistic polymer sample to an entanglement network of PPs. In addition to the set of contour lengths of the PPs and the configuration of the entanglement network, the topological analysis with the Z1 code defines the positions of the interior "kinks"[59,62] along the three-dimensional PP for each chain in the system. For long chains, the number of kinks is proportional to the number of entanglements irrespective of the precise definition of entanglements. It is important to keep in mind, however, that while the structure and average contour length of the entanglement network are robust measures of the topological state of the polymeric system, other quantities (such as the number of kinks) are derived in a postprocessing step, thus good physical intuition is needed for their precise definition.

A few additional points are in order here regarding the Z1-code: (a) The code treats periodic images of the same chain as different chains, while all parts of a physically connected chain (which may cross the border of the simulation box) are

considered as belonging to the same chain. (b) The geometrical minimization procedure terminates as soon as the mean length of all PPs has converged. (c) Self-entanglements are neglected since their number is usually very small and inconsequential for most polymeric systems[56,62] (although a more detailed analysis on the role of self-entanglements may be required for exceedingly long chains). (d) The physically relevant mesh size of the PP network is by definition limited to the periodic box dimension so that finite system-size effects are known to be present if mesh size reaches this limit, cf. ref 62. Accordingly, even if chain dimensions would exceed box dimensions (which is rarely the case for the simulation conditions chosen in this study), finite size effects may be considered irrelevant as long as they are not reflected in the PP network. Systems potentially suffering from finite size effects can still be analyzed using Z1 and tested against finite size effects by investigating periodically replicated simulation cells.

We close this section by mentioning that Z1 shares many similarities with the alternate geometrical method reported in the literature for the topological analysis of polymer melts, the so-called CReTA algorithm. Thus, the main conclusions drawn in this work should not be considered as being specific to the application of the Z1 code. Rather they should be considered as being representative of the more general class of this type of numerical codes (Z1 and CReTA) that identify topological constraints based on geometric operations and transformations.[58,59,69−71]

3. Results and Discussion

3.1. Structural, Rheological, and Optical Properties. *Chain Dimensions.* Figure 1 displays simulation results for the mean-square chain end-to-end distance $\langle R^2 \rangle$ and the mean-square chain radius of gyration $\langle R_g^2 \rangle$ as a function of the imposed shear rate in dimensionless units. At low enough shear rates ($Wi \leq 2$), the two quantities remain practically unaffected by the applied flow, indicating that in this range of shear rates the flow causes mainly orientation (and not distortion) of the chains along the flow direction. At higher shear rates, on the other hand, the values of $\langle R^2 \rangle$ and $\langle R_g^2 \rangle$ increase rapidly with the applied flow; this indicates that for these intermediate flows, polymer molecules are not only aligned along the flow direction but assume also a stretched conformation. This is accompanied by effects such as: (a) significant energetic and entropic contributions to the free energy of the system, (b) development of significant lateral enthalpic interactions between neighboring chains, and (c) development of an anisotropic chain diffusivity tensor, which are all features of the nonlinear viscoelastic response of the melt to the applied flow. At high shear rates, the increase in the chain dimensions gradually slows down, leading eventually to a plateau. An interesting point to make is that the plateau value for $\langle R^2 \rangle$ is only 65 000 Å^2; this is ~25% of the value of 266 000 Å^2 corresponding to the fully stretched chain conformation (for the equilibrium values of the bond lengths and bond bending angles assumed in the simulations, and for the chain in its all-*trans* conformation). This phenomenon (which has also been observed in other simulations[12,38,72,73] and in a number of experimental works[74,75]) is attributed to chain rotation and tumbling under shear.

Another interesting point to make in the results of Figure 1 is that only at equilibrium and small shear rates the simulation data satisfy the relationship $\langle R^2 \rangle = 6\langle R_g^2 \rangle$ valid for Gaussian chains; above $Wi \approx 10$, a significant deviation in the ratio $\langle R^2 \rangle / \langle R_g^2 \rangle$ appears. We can make semiquantitative explanations for this behavior in nonequilibrium states by considering the Porod−Kratky (or worm-like) chain model (see, e.g., Appendix G in ref 5 or Chapter 5 in ref 37), which represents real chains in terms of the persistence length l_p and the maximum chain
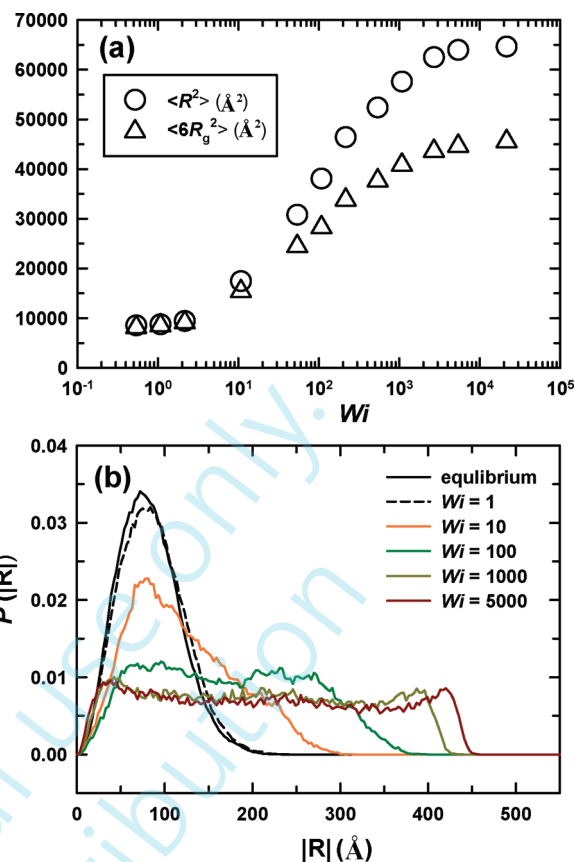

Figure 1. (a) Mean-square chain end-to-end distance $\langle R^2 \rangle$ and mean square radius of gyration $\langle R_g^2 \rangle$ of the simulated $C_{400}H_{802}$ PE melt as a function of shear rate. The equilibrium values are $\langle R^2 \rangle_{eq} = 8014 \pm 200$ Å^2 and $\langle R_g^2 \rangle_{eq} = 1342 \pm 20$ Å^2, respectively. The error bars are smaller than the size of the symbols. (b) Variation of the probability distribution function $P(|\mathbf{R}|)$ for the magnitude $|\mathbf{R}|$ of the chain end-to-end vector with shear rate.

length $R_{\max}$. The model describes the mean-square chain end-to-end distance and its radius of gyration as

$$\langle R^2 \rangle (l_p, R_{\max}) = 2l_p R_{\max} \left\{ 1 - \frac{l_p}{R_{\max}} \left[1 - \exp\left(-\frac{R_{\max}}{l_p}\right) \right] \right\} \tag{7a}$$

$$\langle R_g^2 \rangle (l_p, R_{\max}) = \frac{1}{3} l_p R_{\max} \left\{ 1 - \frac{3l_p}{R_{\max}} + \frac{6l_p^2}{R_{\max}^2} \left[1 - \frac{l_p}{R_{\max}} \left(1 - \exp\left(-\frac{R_{\max}}{l_p}\right) \right) \right] \right\} \tag{7b}$$

In the limit of fully flexible long chains for which $l_p/R_{\max} \to 0$, it is seen that $\langle R^2 \rangle / \langle R_g^2 \rangle$ approaches 6, a well-known result for long flexible polymer chains. In the opposite limit of highly stiff chains for which $l_p/R_{\max} \to \infty$, the following formula can be derived by expanding the exponential terms in the above equations:

$$\frac{\langle R^2 \rangle}{\langle R_g^2 \rangle} = 6 \frac{\left(\frac{1}{2} - \frac{1}{6} \frac{R_{\max}}{l_p} + \cdots \right)}{\left(\frac{1}{4} - \frac{1}{20} \frac{R_{\max}}{l_p} + \cdots \right)} \tag{8}$$

which shows that $\langle R^2 \rangle / \langle R_g^2 \rangle$ should approach 12. We thus see that as chains become less flexible (i.e., a larger value of l_p) at

a given value of R_{max} which is usually characterized by the intrinsic molecular chemistry, the ratio $\langle R^2 \rangle / \langle R_g^2 \rangle$ will be increasing from 6 to 12. Now, turning onto our main point here for nonequilibrium states, polymer chains become more and more stretched and aligned with increasing flow strength, which effectively makes the chains locally stiffer thereby increasing the value of l_p (its nonequilibrium analogue defined through eqs 7a and 7b). It is therefore to be expected that the value of $\langle R^2 \rangle / \langle R_g^2 \rangle$ will increase with the flow strength, which is exactly consistent with the results presented in Figure 1a. Furthermore, in the case of steady shear, both $\langle R^2 \rangle$ and $\langle R_g^2 \rangle$ reach an asymptotic value at high shear rates due to chain rotation, which eventually results in an asymptotic effective value for l_p. This trend is supposed to be valid for other flow types as long as the external flow field increases the chain stiffness by deforming their local and global structures, as has been observed, e.g., in the case of a planar elongational flow (ref 31). Precise descriptions of the chain-length dependence of the ratio as a function of flow strength (including the asymptotic behavior) would, however, be an intricate problem, since the value of l_p is generally a complex function of the flow type and strength as well as of the intrinsic molecular chemistry and architecture. We further conjecture that all these behaviors would be quite independent of both molecular weight M and entanglement molecular weight M_e as long as the length scales of interest are larger than l_p (e.g., $l_p / R_{max} \ll 1$), since l_p can be regarded as independent of M and M_e, as supported by previous NEMD simulation works[30,31,38] on unentangled polyethylene melts.

Figure 1b shows results for the probability distribution function with respect to the magnitude $|\mathbf{R}|$ of the chain end-to-end vector for a number of shear rates in the interval $1 \leq Wi \leq 5000$ covering both linear and nonlinear flow fields. At equilibrium the distribution is Gaussian, in accordance with theoretical predictions for long enough chains. The distribution remains essentially Gaussian even when a flow is applied as long as the dimensionless shear rate is approximately less than 1 (although a small shift of the entire curve to larger $|\mathbf{R}|$ values is clearly discernible in the curves of Figure 1b). For higher shear rates (e.g., for $Wi = 10$ in Figure 1b) the distribution deviates significantly from the Gaussian one, which is consistent with previous simulation reports for shorter (i.e., unentangled) PE melts.[72,73] For example, despite the fact that it is still dominated by a single peak, it is centered asymmetrically around its average value (more precisely, it is broadened on its left). At even higher shear rates (e.g., for $Wi = 100$, 1000, and 5000 in Figure 1b), the distribution becomes very flat in its intermediate region (its width grows considerably); it also shows a tendency to develop two peaks, one at small and one at large $|\mathbf{R}|$ values. This phenomenon is due to chain rotation and tumbling under shear:[72,73,76] the increase in the shear rate enhances the rotational frequency of the molecule (its vorticity), thus also the number of lateral collisions with neighboring chains; consequently the polymer tumbles quickly, since it finds itself more and more often in an unstable orientation relative to the direction of the applied flow. The net result is a chain whose conformation alternates quickly between stretched and collapsed structures, and this explains the broadening of the distribution function for $|\mathbf{R}|$ as well as the appearance of the two peaks (instead of one at low shear rates).[72,73,76–78] To understand quantitatively the enhancement of chain rotation due to shear field, we have calculated the characteristic rotational relaxation time of polymer chains for each shear rate by measuring the time decay of the autocorrelation function of the unit chain end-to-end vector. Results are plotted in Figure 2. At sufficiently low shear rates ($Wi \leq 2$), the relaxation time appears to be almost constant, indicating that the flow effect on chain rotation is relatively small in this regime
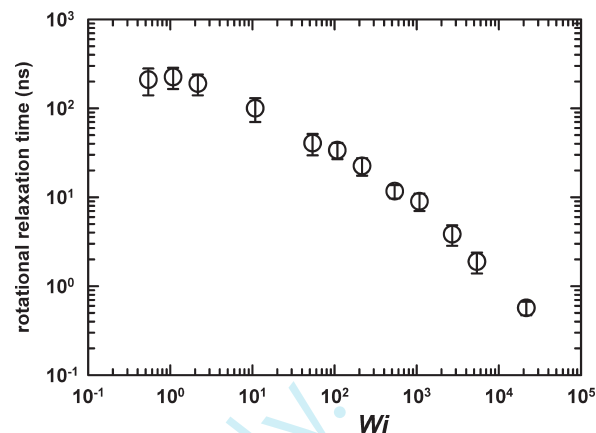

Figure 2. Variation of the rotational relaxation time with shear rate, as calculated by measuring the time decay of the autocorrelation function $\langle \mathbf{u}(t) \cdot \mathbf{u}(0) \rangle$ of the unit chain end-to-end vector $\mathbf{u}$.

as compared to that driven by the random Brownian motion (similar behavior was observed in recent NEMD studies of unentangled polyethylene[72] and polystyrene[50] melts undergoing shear flow). At higher shear rates, however, the relaxation time is shown to decrease dramatically with the flow strength, indicative of a significant enhancement in chain rotation and tumbling by the applied shear field (a similar phenomenon was reported in refs 50 and 72 for shorter sheared polymer melts).

Conformation Tensor. Figure 3 reports results for the variation of the four nonzero components of the conformation tensor ($\tilde{c}_{xx}$, $\tilde{c}_{xy}$, $\tilde{c}_{yy}$, and $\tilde{c}_{zz}$) with the shear rate. The curves obtained are very similar to those already reported in the literature for a number of shorter PE melts from direct NEMD or hybrid GENERIC Monte Carlo/NEMD simulations with a similar atomistic model.[73] More specifically, $\tilde{c}_{xx}$ remains practically constant (close to unity of the equilibrium condition) at low shear rates corresponding to rather weak flows ($Wi \leq 2$), for larger shear rates (corresponding to Weissenberg numbers in the interval $2 \leq Wi \leq 20,000$) it increases rapidly, while for even higher shear rates ($Wi \geq 20,000$) it reaches an asymptote. The overall behavior appears to be quite similar to $\langle R^2 \rangle$ shown in Figure 1a, as $\tilde{c}_{xx}$ dominates over the other components at high shear rates, As closely related to $\langle R^2 \rangle$, the asymptotic behavior of $\tilde{c}_{xx}$ is ascribed to (a) finite chain extensibility due to local bond-stretching and bond-bending interactions, and (b) chain rotation and tumbling under shear flow, which lower the average chain dimension significantly below its maximum value and prevent perfect alignment of chains to the flow (x-) direction;[50] this can also be interpreted as an asymptotic behavior of the persistence length l_p at high shear rates, as described earlier. Qualitatively similar behaviors have also been observed in unentangled polyethylene[38] and polystyrene[50] melts under shear.

$\tilde{c}_{xy}$, on the other hand, increases quickly as the shear rate is increased, goes through a maximum at an intermediate flow strength ($Wi \approx 20$), and then decreases. Its behavior can be understood by taking into account the simultaneous effect of two competing mechanisms:[50] the degree of spatial correlation between the x and y components of the chain end-to-end vector $\mathbf{R}$ which tends to increase $\tilde{c}_{xy}$, and the degree of chain alignment with the flow which tends to decrease $\tilde{c}_{xy}$. Since the detailed quantitative description for these two effects depends on molecular parameters (such as the flexibility or stiffness of the molecule,[50] its linear or branched architecture, and its length), here we can put forward only a qualitative analysis: (a) $\tilde{c}_{xy}$ initially increases at low flow fields where the correlation effect is dominating over chain
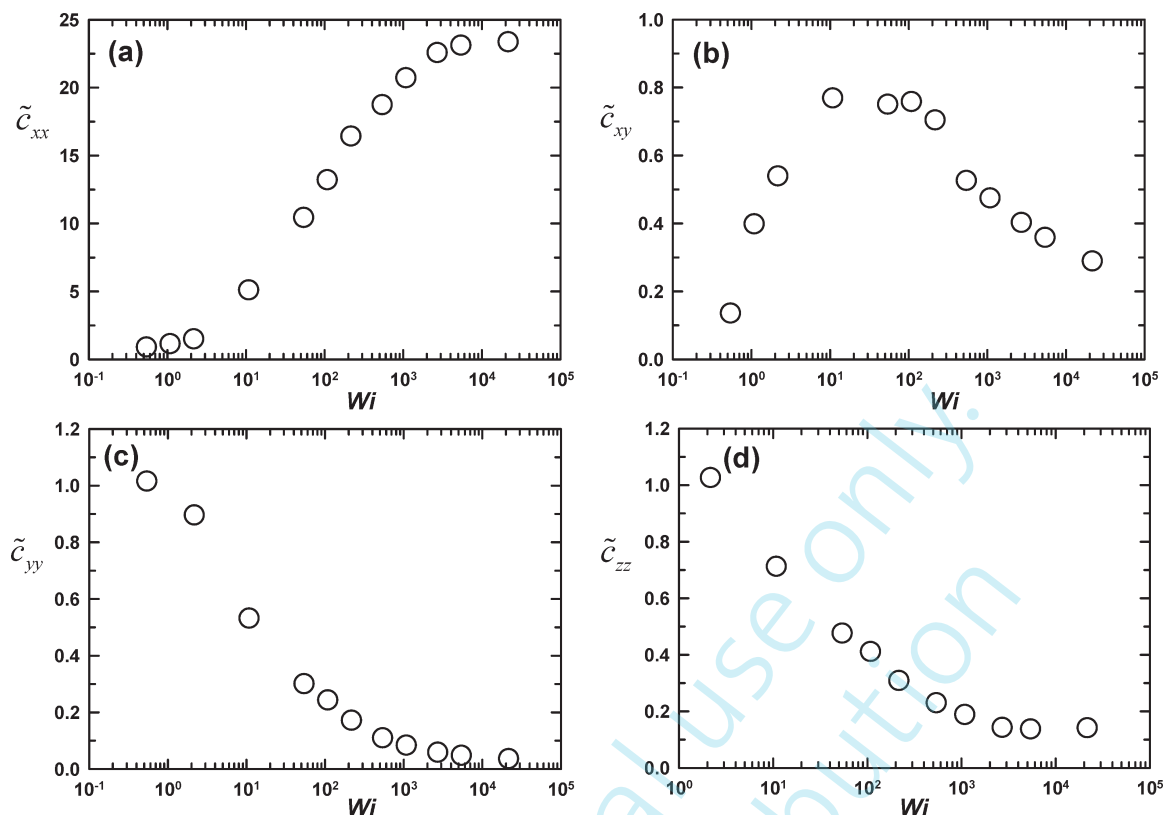
Figure 3. Variation of the nonzero components of the conformation tensor $\tilde{\mathbf{c}}$ with shear rate: (a) $\tilde{c}_{xx}$, (b) $\tilde{c}_{xy}$, (c) $\tilde{c}_{yy}$, and (d) $\tilde{c}_{zz}$. The error bars are commensurate with the size of the symbols.

alignment, (b) its increase slows down at an intermediate range of shear rates where the effect of chain alignment becomes more significant, (c) $\tilde{c}_{xy}$ may exhibit a maximum with further increasing the shear rate, and (d) eventually, $\tilde{c}_{xy}$ reaches an asymptotic value at very high shear rates where both effects are saturated. In the literature, the maximum in the value of $\tilde{c}_{xy}$ with shear rate has also been observed in a recent NEMD simulation study with a model polystyrene melt.[50]

In contrast to $\tilde{c}_{xx}$ and $\tilde{c}_{xy}$, $\tilde{c}_{yy}$, and $\tilde{c}_{zz}$ are found to decrease monotonically with the applied flow, which is physically reasonable given that their behavior is governed solely by the degree of chain orientation and alignment with the flow. Furthermore, $\tilde{c}_{zz}$ decreases more slowly than $\tilde{c}_{yy}$, which should have been expected given that the *y*-axis is the velocity gradient and the *z*-axis is the neutral direction.

Given that the conformation tensor is one of the most favorite primary state variables for the formulation of differential constitutive models,[8,79] the results presented here for its variation with the applied flow can be important not only in getting a deeper understanding of the interplay between flow and molecular-level characteristics of polymer melts but also in developing more accurate rheological models[79−81,36,82,83] and, more importantly, in designing more versatile multiscale simulation methodologies.[36,73,83−85]

Rheological Properties. In Figure 4, we present the predictions of our NEMD simulations for the material functions of the simulated $C_{400}H_{802}$ PE melt, namely the shear viscosity $\eta \equiv -\sigma_{xy}/\dot{\gamma}$, the first normal stress coefficient $\Psi_1 \equiv -(\sigma_{xx} - \sigma_{yy})/\dot{\gamma}^2$, the second normal stress coefficient $\Psi_2 \equiv -(\sigma_{yy} - \sigma_{zz})/\dot{\gamma}^2$, and the ratio $-\Psi_2/\Psi_1$. The results have been obtained by using the following expression for the stress tensor $\boldsymbol{\sigma}$ based on the well-known Irving-Kirkwood statistical-mechanical formula

for homogeneous fluids:[86]

$$\boldsymbol{\sigma} = \left\langle \frac{1}{V} \sum_i \sum_a \left(\frac{\mathbf{p}_{ia}\mathbf{p}_{ia}}{m_{ia}} + \mathbf{q}_{ia}\mathbf{F}_{ia} \right) \right\rangle \quad (9)$$

suitably adapted for systems subject to periodic boundary conditions. In eq 9, V denotes the volume of the system while the angular brackets represent a time average over the system trajectory. Qualitatively, the curves for the rheological properties of the simulated $C_{400}H_{802}$ PE melt reported in Figure 4 are very similar to those measured experimentally for high molecular weight PE melts: For example, in part (a) of the figure we can see the characteristic Newtonian plateau of the shear viscosity at low shear rates ($Wi \leq 1$) and then its monotonic decrease (the so-called shear thinning phenomenon). Our prediction for the Newtonian (or zero-shear) viscosity is $\eta_0 = 0.16 \pm 0.05$ Pa s. This is somewhat smaller than the value of 0.43 Pa s obtained by assuming that $\eta_0 = (\pi^2/12)G_N^0\lambda$ as suggested by the Doi−Edwards model[7] for $G_N^0 = (4/5)\rho RT/M_e \approx 2.4$ MPa (using that $M_e \approx 954$ g/mol based on experimental data[87]). We further see that the degree of shear thinning subsides at the highest shear rates, which is also observed in experiments.[2] By fitting the simulation curve in the shear thinning regime with a power-law expression of the form $\eta \sim \dot{\gamma}^b$, we find that the best curve fits are obtained for $b = -0.89 \pm 0.06$ for shear rates $\dot{\gamma}$ in the interval $10 \leq Wi \leq 200$, and for $b = -0.44 \pm 0.05$ for shear rates corresponding to $Wi \geq 500$. Typical values with linear PE melts reported in the literature from experimental measurements[2] suggest that in general $-0.9 \leq b \leq -0.4$.

Parts b and c of Figure 4 show our simulation results for the two normal stress coefficients Ψ_1 and Ψ_2 as a function of dimensionless shear rate. Consistent with experimental observations,[2] both exhibit a large shear thinning behavior which is captured quite well by the following two power-law expressions: (a) $\Psi_1 \sim \dot{\gamma}^b$ with $b = -1.65 \pm 0.05$ for $10 \leq Wi \leq 200$, and
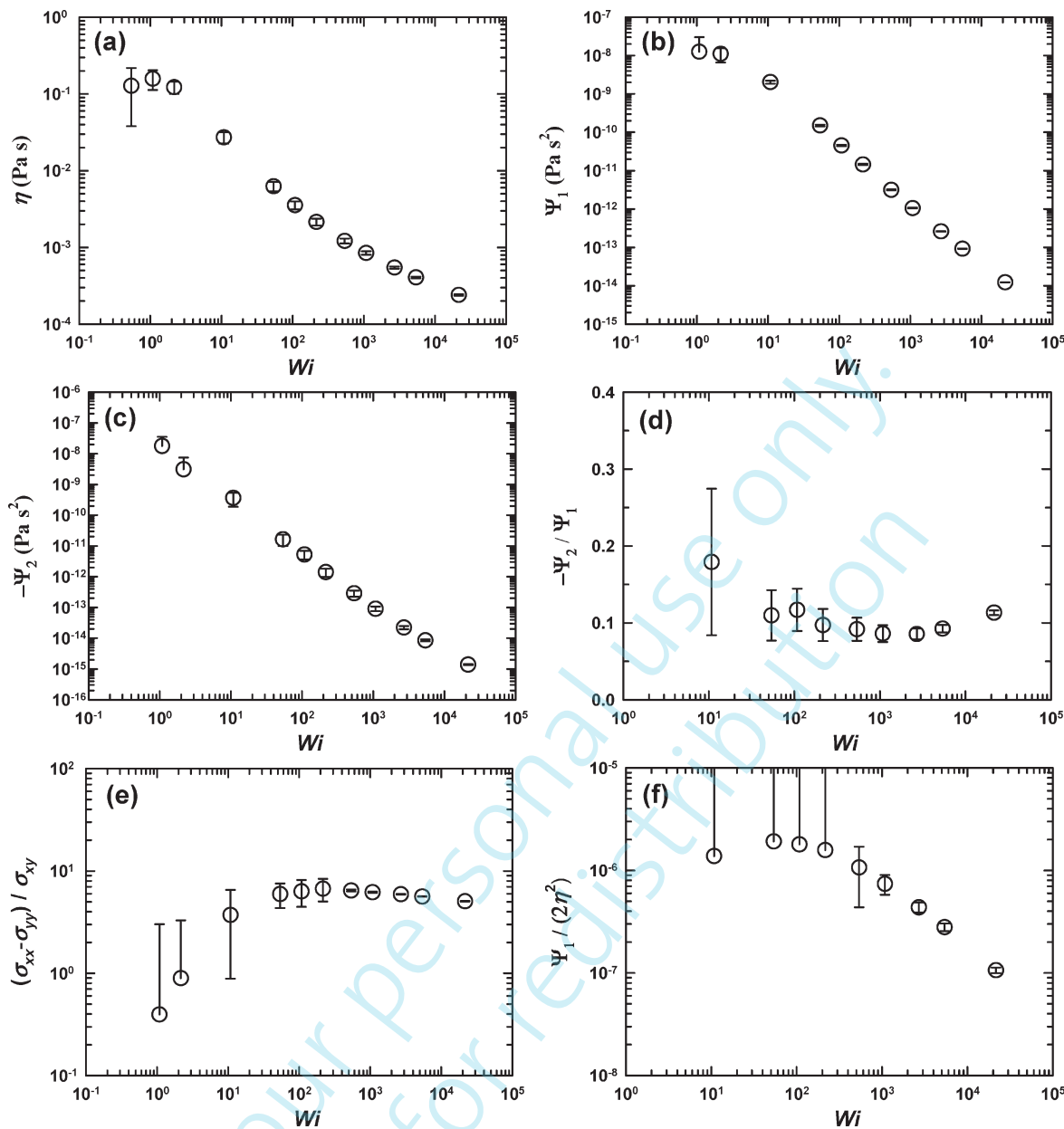
Figure 4. NEMD simulation predictions for the steady-state viscoelastic material functions of the simulated $C_{400}H_{802}$ PE melt: (a) the shear viscosity η, (b) the first normal stress coefficient Ψ_1, (c) the second normal stress coefficient Ψ_2, (d) the ratio $-\Psi_2/\Psi_1$ of the second to the first normal stress coefficient, (e) the ratio of the first normal stress difference to the shear stress, and (f) the nonequilibrium shear compliance.

$b = -1.50 \pm 0.06$ for $Wi \geq 500$, and (b) $\Psi_2 \sim \dot{\gamma}^b$ with $b = -1.85 \pm 0.09$ for $10 \leq Wi \leq 200$, and $b = -1.44 \pm 0.12$ for $Wi \geq 500$. In Figure 4d, where we report the ratio $-\Psi_2/\Psi_1$, we see that $0.09 \leq -\Psi_2/\Psi_1 \leq 0.18$; typical experimental data[2,7] for linear PE suggest that $0.05 \leq -\Psi_2/\Psi_1 \leq 0.3$. Figure 4e presents the variation of $(\sigma_{xx} - \sigma_{yy})/\sigma_{xy}$ with $\dot{\gamma}$; this is representative of the ratio between material elasticity and material viscosity for the polymer melt under study. As expected, for weak flows, the viscous component dominates and the ratio $(\sigma_{xx} - \sigma_{yy})/\sigma_{xy}$ comes out to be relatively small. For stronger flows, on the other hand, the elastic character becomes more and more important. A similar picture emerges based on experimental observations reported in the literature (see, e.g., ref 2, p. 112). Lastly, in Figure 4f, we plot the dependence of the nonequilibrium shear compliance $J_e = \Psi_1/(2\eta^2)$ for the simulated $C_{400}H_{802}$ PE melt on Wi: according to the simulation results, for low-to-intermediate shear rates, J_e (which always attains small values) remains approximately constant. For higher shear rates

(above about $Wi = 200$) however, it starts decreasing following to a good approximation the scaling $J_e \sim \dot{\gamma}^{-0.63 \pm 0.06}$.

Of interest is also the variation of the hydrostatic pressure P developing in the simulated system as a function of the applied Wi number. P is calculated as one-third of the trace of the stress tensor

$$P = \frac{1}{3}(\sigma_{xx} + \sigma_{yy} + \sigma_{zz})$$

and its dependence on Wi is displayed in Figure 5. It remains almost constant at low enough shear rates (for Wi numbers less than approximately 3), then starts to drop fast as Wi increases up to values approximately equal to 5000, and eventually reaches a plateau (a minimum). A similar behavior has been reported in previous NEMD simulations with short linear and branched PE melts undergoing shear[12,32,88] or planar elongation flow,[30,31] and can be explained by
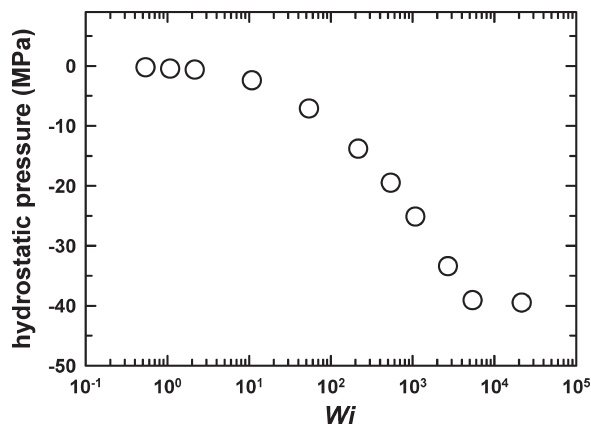
Figure 5. Hydrostatic pressure P versus Wi. The error bars are smaller than the size of the symbols.

considering the two competing effects also discussed above.[12,30-32] The first is related to the increase in chain alignment and stretching with the flow as the applied shear rate is increased, which increases lateral interactions between molecules and enhances attractive (i.e., negative) contributions to the value of the potential energy function, causing a decrease in the pressure. The second is related with the increase in the number and frequency of dynamical intermolecular collisions between molecules,[30-32] which together with chain rotation[72-75] results in an increase in the hydrostatic pressure as the shear rate is increased. Our simulation results therefore indicate that chain alignment and stretching dominate molecular collisions and chain rotation up to a certain (and rather high) value of $\dot{\gamma}$ beyond which, however, as the degree of chain alignment and stretching is saturated, molecular rotation and collisions become the dominant mechanisms. These latter phenomena lead to the observed plateau in Figure 5 at the highest Wi numbers studied here by our NEMD code. Incidentally, it is useful to note that the decrease of the pressure is mainly caused by the decrease in the normal stress σ_{xx} in the flow (x-) direction, which can be interpreted as indicative of an increased retracting force against an effective tensile force (created by the applied flow field) acting on the chains.

Flow Birefringence. In Figure 6, we present the simulation results for the flow birefringence tensor as a function of the applied stress tensor. The birefringence tensor can be calculated by using the following generalized formula of the Lorentz-Lorenz equation in optics:[89,90]

$$\alpha = \frac{3\varepsilon_0}{\tilde{N}}(\mathbf{n}\cdot\mathbf{n}+2\mathbf{I})^{-1}\cdot(\mathbf{n}\cdot\mathbf{n}-\mathbf{I}) \tag{10}$$

In eq 10, ε_0 denotes the permittivity of vacuum, $\tilde{N}$ the polymer number density, α the polarizability tensor, $\mathbf{I}$ the second-rank unit tensor, and $\mathbf{n}$ the birefringence tensor. How eq 10 should be used in order to determine the birefringence of computer generated atomistic polymer samples subjected to flow is described in detail by Mavrantzas-Theodorou[89] and Baig et al.[90] Figure 6a displays the plot of n_{xy} vs σ_{xy} for the simulated $C_{400}H_{802}$ PE melt. For stresses up to $-\sigma_{xy} \approx 1.7$ MPa (obtained for $Wi \approx 100$), a linear relationship is observed between n_{xy} and σ_{xy} known as the stress-optical rule (SOR); beyond this stress value, n_{xy} changes with σ_{xy} nonlinearly. An important point to make here is that the highest Wi number (≈ 100) for which the stress optical rule holds is considerably larger than the Wi number (≈ 2) for which the shear thinning behavior of the viscosity shows up.
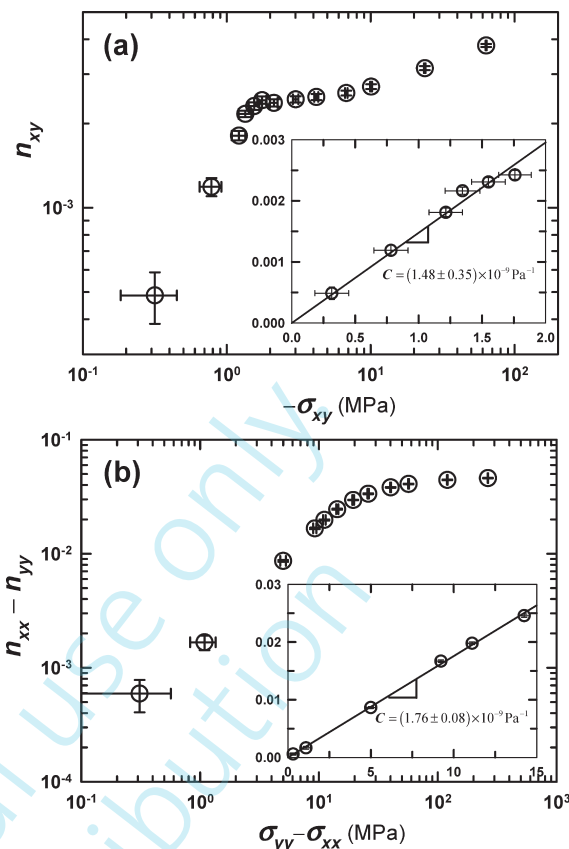

Figure 6. Relationship between birefringence tensor $\mathbf{n}$ and stress tensor $\boldsymbol{\sigma}$: (a) η_{xy} versus σ_{xy}, and (b) $n_{xx} - n_{yy}$ versus $\sigma_{xx} - \sigma_{yy}$. In the inset, we have emphasized the regime where the stress-optical rule holds (the corresponding slopes define the stress-optical coefficient C).

Qualitatively similar results have been observed in NEMD simulations with two shorter ($C_{50}H_{102}$ and $C_{128}H_{258}$) linear PE melts.[12,90] We also note the recent experimental work of Luap et al.[91] where a value of shear stress equal to ≈ 2.7 MPa was found to mark the break of the stress optical rule for a polystyrene melt subjected to uniaxial elongation. The stress-optical coefficient (i.e., the slope in the linear part of the n_{xy}-vs-σ_{xy} plot) C is found to be equal to $(1.48 \pm 0.35) \times 10^{-9}$ Pa^{-1}, which should be compared to the value of 2.35×10^{-9} Pa^{-1} measured experimentally for a high molecular weight, high-density PE melt at $T = 423$ K.[92]

A linear relationship at small enough stress values is also observed (see Figure 6b) if one plots $n_{xx} - n_{yy}$ versus $\sigma_{yy} - \sigma_{xx}$ (see also ref 12). The SOR appears to be valid up to a certain value of the first normal stress difference approximately equal to $\sigma_{yy} - \sigma_{xx} \approx 14$ MPa (obtained for $Wi \approx 200$), beyond which it breaks down. The corresponding coefficient C in the linear part of the plot comes out to be equal to $(1.76 \pm 0.08) \times 10^{-9}$ Pa^{-1}, which is somewhat different from the value $(1.48 \pm 0.35) \times 10^{-9}$ Pa^{-1} reported above from the n_{xy}-vs-σ_{xy} plot.

Alignment Angle and Order Parameter. In Figure 7, we report our simulation data for the effect of the applied shear flow on the degree of chain alignment/orientation and ordering with the flow. Part a of the figure shows three different measures of the degree of chain alignment based on the angle formed between the flow direction and a director which is taken here to be represented by the eigenvector corresponding to the largest eigenvalue of one of the following three second-rank tensors:[39] (a) the order (or orientational) tensor $\mathbf{S} = \langle(3\mathbf{uu} - \mathbf{I})\rangle/2$ where $\mathbf{u}$ denotes the unit chain end-to-end vector, (b) the birefringence tensor $\mathbf{n}$, and (c) the stress tensor $\boldsymbol{\sigma}$. First, we note that near
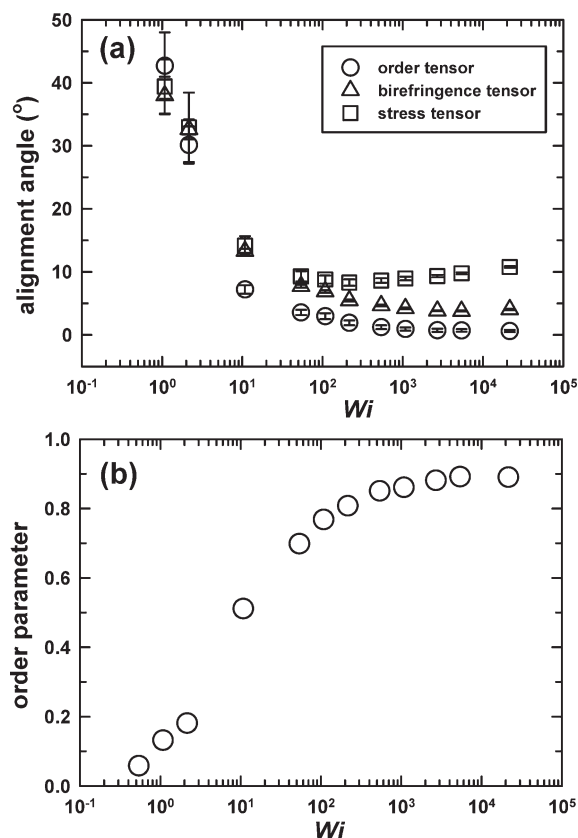
Figure 7. (a) Variation of the alignment angle with *Wi*. Three sets of data are shown corresponding to the following three different tensors: the order (or orientational) tensor $\mathbf{S} = \langle (3\mathbf{uu} - \mathbf{I}) \rangle / 2$ where $\mathbf{u}$ is the unit chain end-to-end vector and $\mathbf{I}$ the second-rank unit tensor, the birefringence tensor $\mathbf{n}$, and the stress tensor $\boldsymbol{\sigma}$. (b) Variation of the order parameter (the largest eigenvalue of the order tensor $\mathbf{S}$) with *Wi*.

equilibrium (very small *Wi* numbers) the alignment angle as calculated from all these three tensors approaches the value of 45°, exactly as should have been expected based on simple theoretical arguments for the shape of these tensors in the limit of zero flow (chains should be neither stretched nor elongated in any preferred direction although a nonzero *xy*-component should be present). On the other hand, as the shear rate is increased, the chains become more and more stretched (also more and more aligned) along the flow direction, which decreases significantly the value of the alignment angle. It is in fact interesting that for *Wi* numbers up to approximately 100 (which is far away from the incipient point of shear thinning), the alignment angles computed from the birefringence and stress tensors are practically identical (a direct consequence of the stress optical rule for the linear relationship between the two tensors). For *Wi* numbers larger than about 100, the results of Figure 7a indicate different values for the alignment angle from the three different tensors: consideration of the stress tensor results in the largest angles, consideration of the order tensor results in the smallest angles, and consideration of the birefringence tensor results in intermediate angles. In fact, it seems that consideration of the stress tensor results in alignment angles which go through a shallow minimum at an intermediate value of the *Wi* number (approximately equal to 200), which most probably should be attributed to effects such as molecular collisions (that are quite enhanced at these high shear rates). Another interesting point is the deviation in the values of the alignment angle represented by the order and birefringence tensors (**S** and **n**, respectively) even at relatively small fields (e.g., at *Wi* ≈ 10), indicative of significant quanti-

tative differences in the melt structure and degree of ordering at small (bonds) and large (chain end-to-end distance) length scales. (Incidentally, this deviation becomes smaller by further increasing the shear rate, implying a stronger flow effect on local chain scales at higher flows.) All of them are demonstrations of the richness of the dynamical phenomena accompanying the application of a flow on macromolecular liquids owing to the tremendous multiplicity of characteristic length and time scales present in these systems.

In Figure 7b, we report the variation of the chain order parameter (corresponding to the largest eigenvalue of **S**) with the applied flow field. Clearly, the degree to which chains get ordered along the flow direction increases with increasing shear rate, approaching a plateau (~0.9) at high enough fields where approximately 90% of the chains (on the average) is supposed to be aligned along the flow direction. Here we should be cautious not to be confused with the results for $\langle R^2 \rangle$ in Figure 1 which turned out to be only ~25% of its maximum value at the highest shear rates. Mathematically, the order parameter represents the degree of chain ordering around the director. Specifically, the order parameter is quantitatively equivalent to

$$\langle P_2 (\cos \theta) \rangle = \frac{1}{2} (3 \langle \cos^2 \theta \rangle - 1)$$

where θ is the angle between $\mathbf{u}$ and the director. Therefore, the order parameter is directly related to the variance of the probability distribution function of the chain alignment along the director (represented by the average orientation angle in Figure 6a), rather than the absolute magnitude of chain dimension $\langle R^2 \rangle$ or $\langle R_g^2 \rangle$. For instance, for a rod-like polymer dealt with in many liquid crystals, the order parameter can vary significantly with the flow yet the chain dimension remains constant. Meanwhile, it is possible that chains can be better aligned to the director when they become more stretched by the flow field, through the larger torque (the higher free energy in a thermodynamic sense) imposed on them at their unstable orientational states.

Potential Energies. The variation of the total potential energy and of three of its components (torsional, LJ intramolecular and LJ intermolecular) for the simulated $C_{400}H_{802}$ PE system as a function of the *Wi* number is shown in Figure 8. The overall results obtained here bear certain similarities to those reported in the literature in the recent past from NEMD simulations with other, shorter PE melts (see, e.g., refs 12 and 38), so only a brief account will be given here. The total potential energy changes very little at small shear rates (i.e., *Wi* ≤ 2) but decreases significantly if the shear rate exceeds a specific value (Figure 8a); this phenomenon is mainly attributed to the increment in chain alignment and stretch with the applied flow. A more detailed understanding can be gained by looking separately into the individual potential energy contributions from the various interaction modes. Figure 8b shows the change (decrease) in torsional energy with shear rate, revealing an enhancement of *trans*-conformational states with the flow. In Figure 8c, we have plotted the change in the intramolecular LJ energy with *Wi*. The figure shows an increase with the shear rate up to a certain *Wi* number (≈200), beyond which a decrease is observed. This phenomenon can be understood by considering the effects of chain stretching and chain rotation: favorable (corresponding to negative values) intramolecular LJ interactions are initially diminished as the applied flow results in larger interatomic separations along a given chain due to chain stretching. But as the shear rate is increased even further, chain rotation and chain tumbling effects become the dominant mechanisms causing chains to assume rather compact
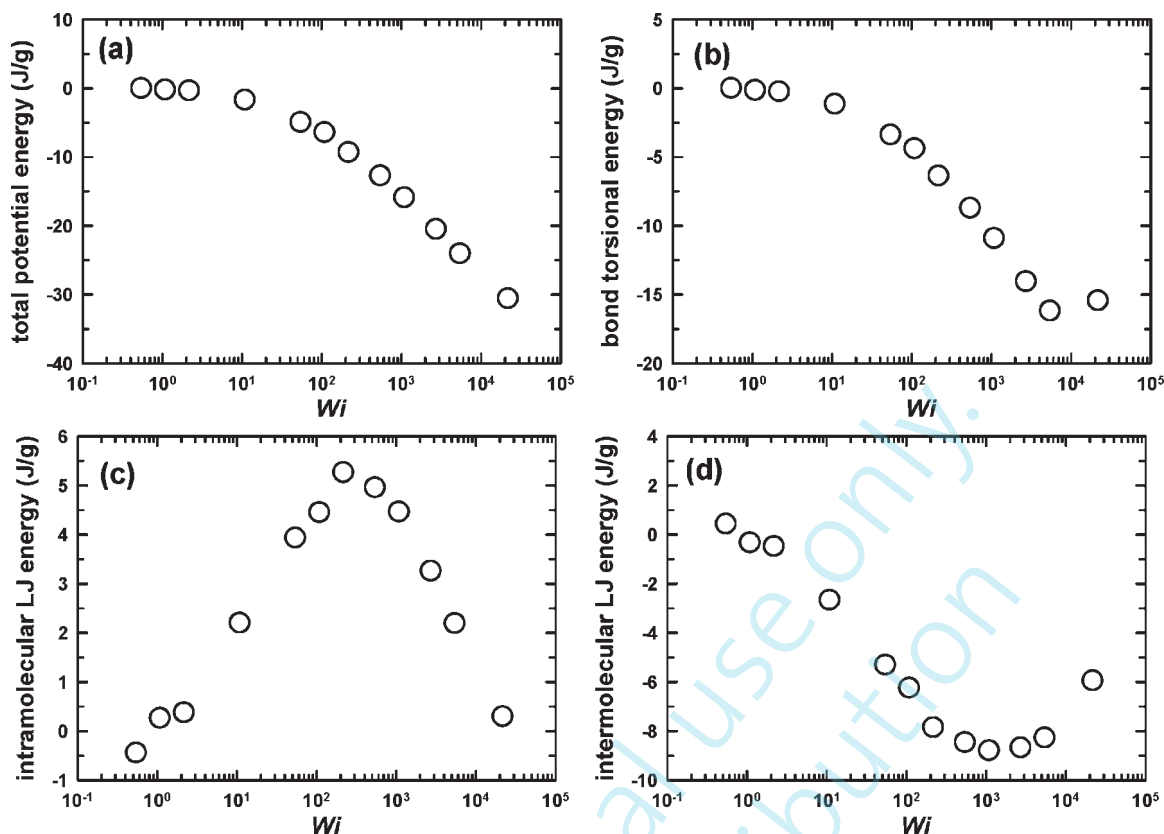
Figure 8. Variation of the potential energy of interaction between atomistic units (relative to equilibrium) with applied shear rate: (a) total potential energy, (b) bond-torsional energy, (c) intramolecular LJ energy, and (d) intermolecular LJ energy.

(collapsed) conformations resulting in smaller interatomic distances along the chain. By comparison, the intermolecular LJ energy decreases initially with increasing the shear rate, passes through a shallow minimum, and then increases with a further increase in shear rate (Figure 8d). The initial decrease of the intermolecular LJ energy with increasing flow strength mainly results from the increase of the favorable (negative) interaction area between chains, as chains are better aligned (i.e., higher ordering) with each other with more stretched conformation. The subsequent increase is attributed to the significant increase of dynamical molecular collisions at high flow fields. It is further seen that the intermolecular LJ energy overcompensates for the loss in favorable intramolecular interactions. Similar behaviors for the intermolecular and intramolecular LJ energies have been observed in unentangled PE melts under shear[12,38] and planar elongational flow.[30,31] If the flow strength increased beyond the maximum shear rate considered here, dynamical effects associated with intermolecular collisions between chains will eventually dominate resulting in an increase of the total potential energy, which has been observed for short PE melts under strong flow fields (see refs 12, 30, 31, and 38).

Of interest is the dependence on shear rate of the bond torsional energy, which is very similar to that of the hydrostatic pressure discussed in Figure 5 (and to some extent to that of the intermolecular LJ energy). This indicates that the pressure in the system is closely associated with the overall chain conformation or shape; a similar phenomenon has been reported in a recent NEMD study of an unentangled H-shaped PE melt.[12] We further report that the bond stretching and bond bending energies barely change (by ∼1 J/g) over the entire regime of Wi numbers examined here.

Radial Pair Distribution Function. In Figure 9, we compare the intermolecular part of the pair distribution function, $g_{inter}(r)$, for four different values of the Wi number: $Wi = 0$
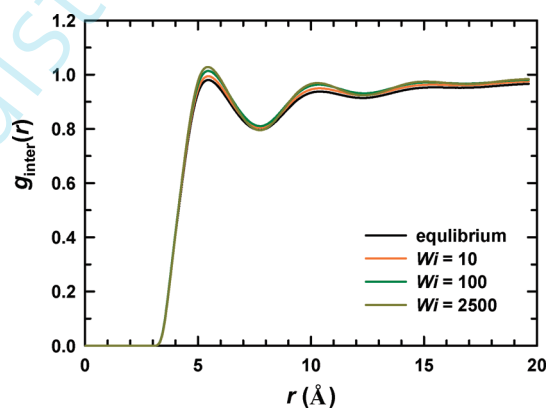

Figure 9. Flow field effects on the structure of the simulated $C_{400}H_{802}$ PE liquid based on the intermolecular part of the pair distribution function $g(r)$. The plots at low shear rates ($Wi < 2$) were practically identical to those at equilibrium.

corresponding to a melt under no flow (i.e, under equilibrium) conditions, $Wi = 10$ corresponding to a weak or intermediate flow, $Wi = 100$ corresponding to a rather strong flow, and $Wi = 2500$ corresponding to a very strong flow. [$g_{inter}(r)$ plots for Wi numbers less than approximately 2 were almost indistinguishable from the equilibrium one.] The results shown in Figure 9 have the typical shape of the pair intermolecular distribution function $g_{inter}(r)$ known in general for polymeric liquids. In addition, as the flow strength is increased: (a) the characteristic peaks in the $g_{inter}(r)$ plots become more pronounced, and (b) the positions of the peak shift slightly to the left; both of these observations are indicative of a flow-enhanced packing of the atomistic units in the simulated melt. We also point out the more intensified
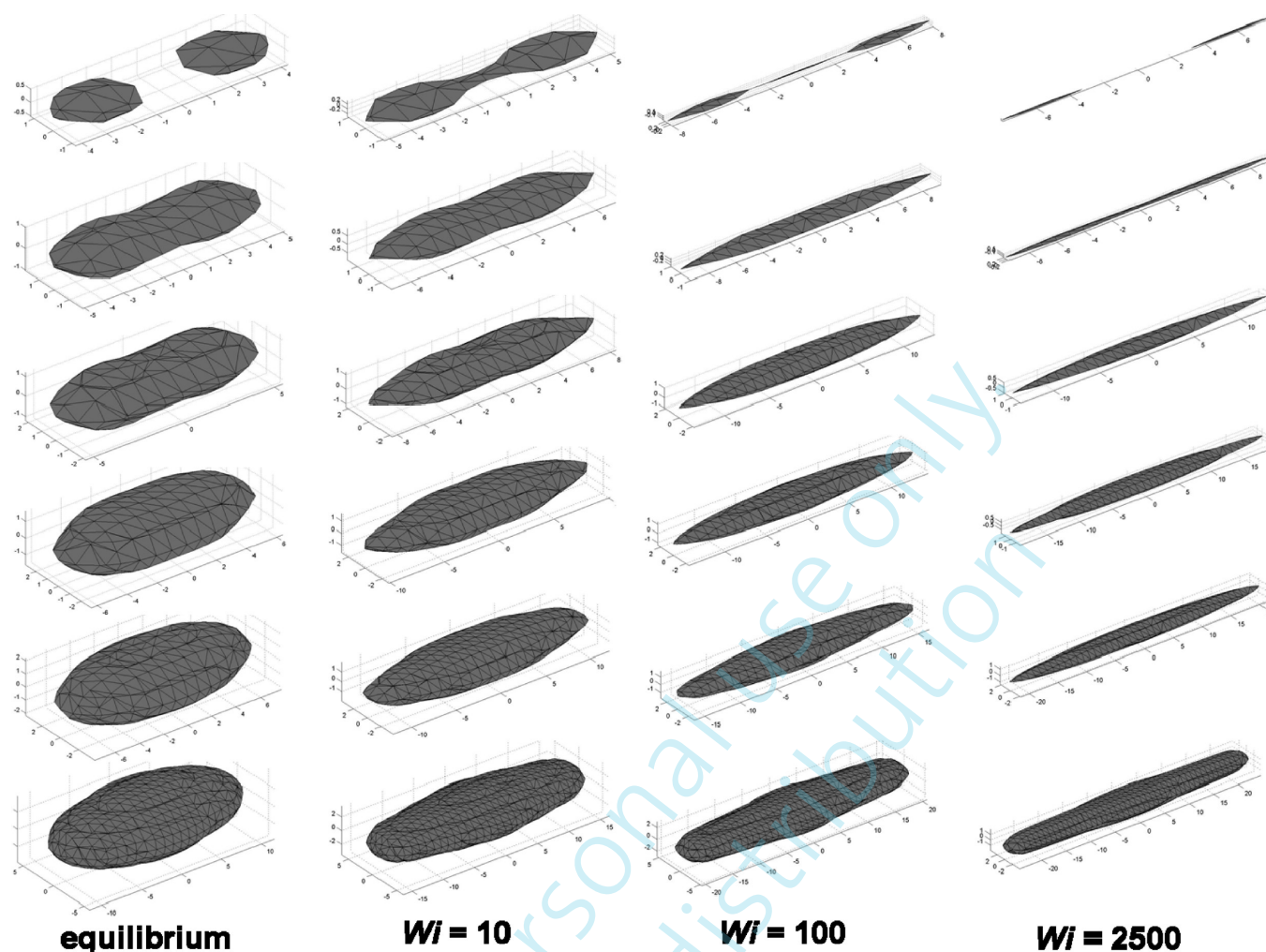
Figure 10. Comparison of the intrinsic molecular shape of a $C_{400}H_{802}$ PE molecule at different shear rates: (a) $Wi = 0$ (i.e., at equilibrium), (b) $Wi = 10$, (c) $Wi = 100$, and (d) $Wi = 2500$. The isosurface plots have been computed at equal values of the average monomer number density in the frame of the principal axes (corresponding to the three eigenvectors) of the instantaneous radius of gyration tensor for each chain. For each state point, the pictures from bottom to top represent the molecular shape including 99, 80, 60, 40, 20, and 10% of the total number of monomers, respectively.

oscillatory behavior of $g_{inter}(r)$ with the flow strength which indicates an enhancement of structural and spatial correlations between chains; this has been quantitatively reported in an NEMD study of a sheared soft-disk fluid,[93] by introducing a long-range potential representative of the nonequilibrium fluid structure.

Intrinsic Molecular Shape. Significant information about the structural changes induced by the applied flow can be obtained by investigating changes in the intrinsic molecular shape of the $C_{400}H_{802}$ PE chains as a function of the applied shear flow. Typical graphs are reported in Figure 10 showing isosurface plots computed at equal values of the average monomer (or segment) number density[94] in the frame of the principal axes (corresponding to the three eigenvectors) of the instantaneous radius of gyration tensor for each chain at four different Wi numbers: (a) $Wi = 0$, (b) $Wi = 10$, (c) $Wi = 100$, and (d) $Wi = 2500$. What are shown in Figure 10 at each one of these four state points are the segment clouds including 99, 80, 60, 40, 20, and 10% of the total number of monomers, respectively. At equilibrium, the intrinsic molecular shape corresponding to 99% segment density resembles a "cake of soap" instead of being an isotropic sphere or ellipsoid, in full consistency with the theoretical predictions of Šolc and Stockmayer[95] based on random walk chains and the Monte Carlo numerical results of Theodorou and Suter[96] based on the rotational isomeric state

model for unperturbed polypropylene chains. As the segment density increases, the middle parts of the shape become thinner and thinner compared to the parts near the ends, and eventually the entire shape breaks down to two distinct core parts.[96] At $Wi = 10$, it is seen that (a) the overall shape looks more elongated and thinner and (b) the middle parts of the shape appear to be flatter and the near-end parts look sharper; this phenomenon can be understood again by taking into account the chain rotation and tumbling (leading to a periodic chain collapse and thus to a fatter middle part) and the chain stretch (leading to more uniform segment distribution along the chain) effects accompanying shear at higher rates. By further increasing the shear rate, the phenomenon becomes more and more pronounced, as can be nicely observed by the shapes of the clouds reported in Figure 10 for $Wi = 100$ and $Wi = 2500$. For a more thorough discussion of flow effects on the intrinsic molecular shape of polymer molecules and how this is affected by the presence of branch points along the chain, we refer the interested reader to a recent publication, ref 12.

3.2. Topological Measures. We turn our attention now to a number of topological measures for the entanglement network underlying the simulated $C_{400}H_{802}$ PE melt. As mentioned above, the reduction of atomistic configurations to a network of PPs has been carried out with the Z1 algorithm, a method that invokes a set of geometric operations in order
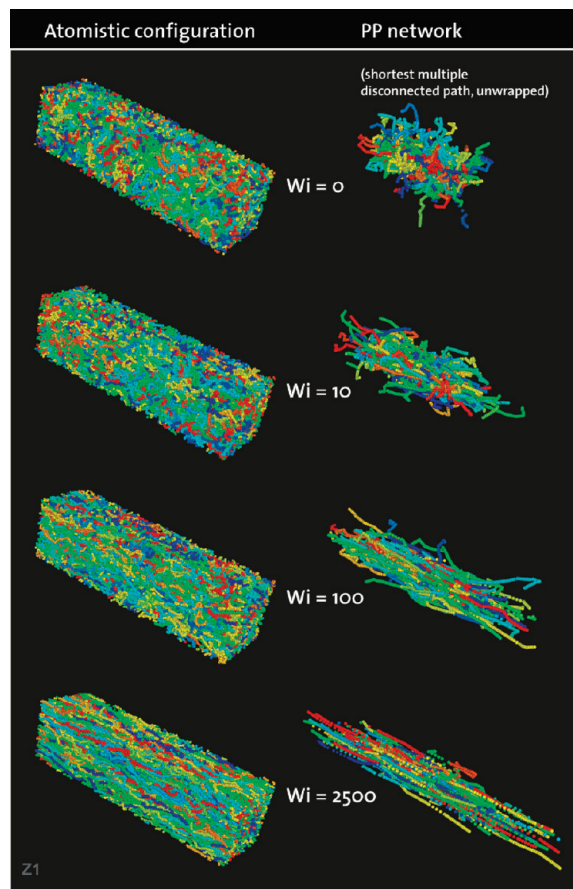
Figure 11. Representative atomistic snapshots (left) and the corresponding PP networks (right) of the simulated $C_{400}H_{802}$ PE liquid at various shear rates (from top to bottom: $Wi = 0$, $Wi = 10$, $Wi = 100$, and $Wi = 2500$).

Figure 12. (a) Probability distribution function $P(L_{pp})$ for the PP contour length L_{pp} as a function of shear rate. (b) Variation of the average value $\langle L_{pp} \rangle$ with shear rate.

to obtain the shortest multiple disconnected path solution to the PP problem. Figure 11 provides representative snapshots of the simulated $C_{400}H_{802}$ PE melt and of the corresponding PP network structures at four different Wi numbers: $Wi = 0$, $Wi = 10$, $Wi = 100$, and $Wi = 2500$. Admittedly, the applied flow has a strong effect on melt structure: as the shear rate is increased, the chains become more and more aligned and stretched along the flow (*x*-) direction. The effect of flow is also (and more) discernible at the level of the entanglement network underlying the topology of the simulated melt: Following the applied flow, the entanglement strands making up a PP tend to orient with the flow, a behavior which is more pronounced at the higher Wi numbers resulting in PPs which have the shape of rods pointing almost perfectly to the direction of the flow. Clearly, the system possesses a different topology at different Wi numbers. We examine this in more quantitative terms below by showing how the flow affects the distribution of entanglement points along a PP, the spacing between entanglements, and the contour length of PPs.

Primitive Path Contour Length. Our NEMD results for the probability distribution function $P(L_{pp})$ of the PP contour length L_{pp} as a function of applied shear rate are shown in Figure 12a. At equilibrium ($Wi = 0$), the distribution is practically Gaussian. The same is true also at low shear rates (e.g., up to $Wi = 2$): the distribution is again Gaussian but slightly shifted to the right indicating relatively higher L_{pp} values compared to those in the absence of flow. The peak of the distribution is also slightly reduced. As the shear rate is increased corresponding to higher Wi numbers, the distribution becomes more and more nonsymmetric with respect to its most pro-
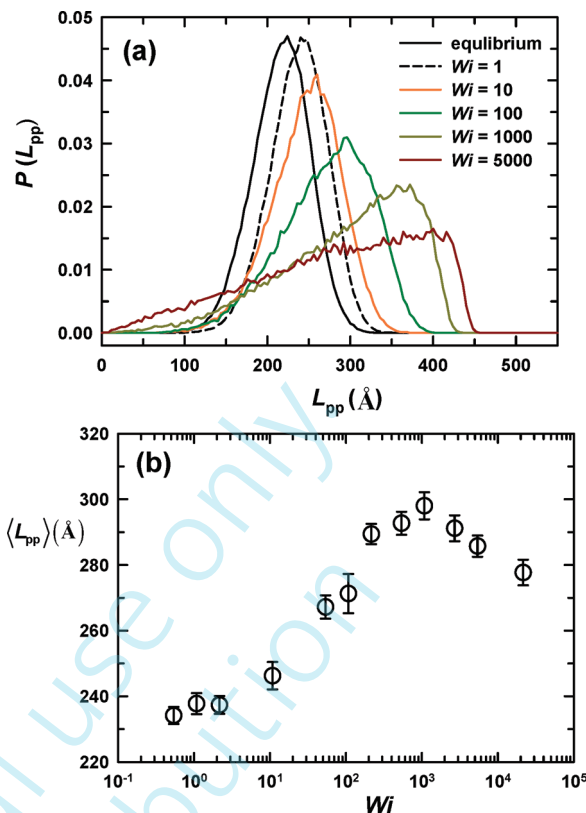
bable value indicating significant deviations from the Gaussian shape. The overall results resemble to some extent those presented in Figure 1b for the distribution $P(|\mathbf{R}|)$ of the magnitude $|\mathbf{R}|$ of the chain end-to-end vector at high enough Wi numbers: (a) chains get significantly extended along the flow direction (chains assume longer dimensions due to the applied strong flow), which causes the shift of the peak of the distribution to larger L_{pp} values; and (b) the rate (i.e., frequency) of chain rotation and tumbling is also enhanced, which results in the development of an asymmetric distribution around its peak (a distribution that is broader on the left of the peak).

The corresponding results for the effect of the shear flow on the average value, $\langle L_{pp} \rangle$, of the PP contour length are shown in Figure 12b. Starting from the value of 227 ± 7 Å at equilibrium, the figure shows that $\langle L_{pp} \rangle$ increases rather fast with increasing Wi number, it reaches a maximum at approximately $Wi \approx 1000$, and then starts decreasing. This behavior, especially the maximum at a certain (high enough) Wi number, is explained by considering the following two competing effects as Wi is increased: (a) the increase (on the average) of the chain dimensions which tends to increase $\langle L_{pp} \rangle$, and (b) the decrease in the degree of topological interactions (or the number of entanglements; see also Figure 13b) as chains are aligned more and more with the flow which tends to decrease $\langle L_{pp} \rangle$. Here, it is instructive to contrast our NEMD results for the variation of $\langle L_{pp} \rangle$ shown in Figure 12b with the applied flow to those for the variation of $\langle R^2 \rangle$ shown in Figure 1a; while the asymptotic value of $\langle R^2 \rangle^{1/2}$ at high shear rates is approximately three times ($\sim 300\%$) larger than the equilibrium one, the maximum value of $\langle L_{pp} \rangle$ occurring at $Wi \approx 1000$ is only by about 40% larger than the corresponding equilibrium value. We therefore understand that the assumed ($\sim 300\%$) increase in $\langle L_{pp} \rangle$ associated with the
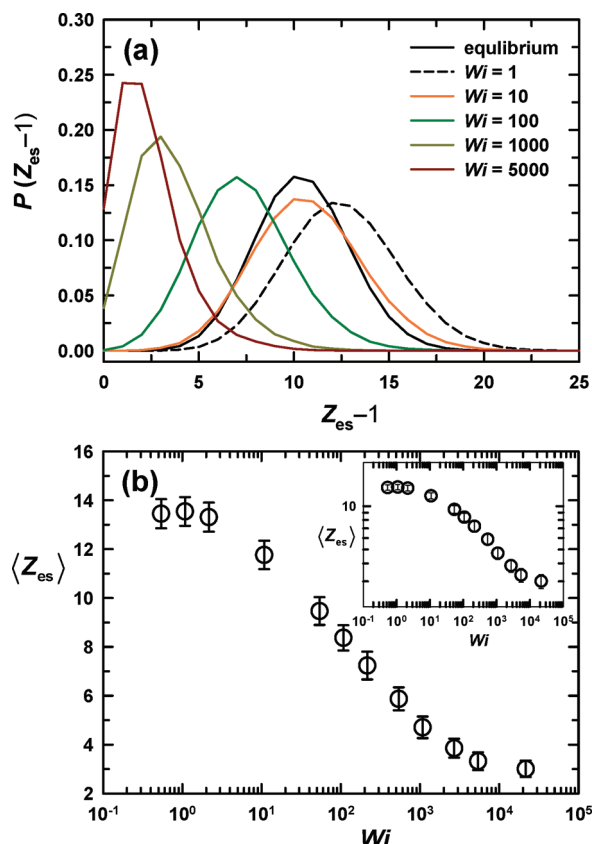
Figure 13. Same as with Figure 12, but for the number Z_{es} of entanglement strands per chain.

increase of $\langle R^2 \rangle^{1/2}$ is largely compensated by the loss of topological interactions due to chain alignment.

Overall, we conclude that the PP contour length is affected by the imposed shear field in a rather complicated way due to effects associated with chain extension and chain alignment that act in opposite directions; on the basis of the results shown in Figure 12b, the former effect dominates over the latter up to $Wi \approx 1000$, beyond which the latter effect dominates over the former (it is informative for quantitative understanding to compare the results between Figures 1 and Figure 13b). These two effects are also behind the distortion from the Gaussian shape of the probability distribution $P(L_{pp})$ for L_{pp} at high low fields.

Number of Entanglements Per Chain. In Figure 13a, we present our NEMD data for the variation of the probability distribution function $P(Z_{es})$ for the number Z_{es} of entanglement points per chain with the applied flow. We first note that at equilibrium $P(Z_{es})$ follows a Poisson distribution (very similar to the Gaussian one for large values of the mean), which is consistent with a previous analysis[61] of linear PE melts generated in the course of MC simulations with chain connectivity altering algorithms; it is also in accordance with analytical theories.[97] $P(Z_{es})$ follows also a Poisson distribution at low shear rates (corresponding to Wi numbers approximately less than about 10), except from a small shift to the right (slightly larger Z_{es} values). But as the shear rate is increased even further (corresponding to Wi numbers above approximately 10), the $P(Z_{es})$ curves are seen to move to smaller $\langle Z_{es} \rangle$ values characteristic of smaller and smaller entanglement points per chain. In fact, at very high shear rates (corresponding to Wi numbers approximately above 1000), $P(Z_{es})$ attains a non-negligible value for $Z_{es} = 1$, revealing the existence of many chains completely devoid of entanglements. This indicates that at very high shear rates a

significant number of chains are not entangled with other chains, which in turn implies chains with a collapsed overall structure under these strong flows. Note though that, even in these very high flow fields, $P(Z_{es})$ remains still Poisson-like.

The average number of entanglement strands per chain, $\langle Z_{es} \rangle$, as a function of shear rate is shown in Figure 13b. $\langle Z_{es} \rangle$ is a very significant topological measure, since it is indicative of the degree of topological interactions in the system under study. According to the data of Figure 13b, $\langle Z_{es} \rangle$ at low shear rates (corresponding to Wi numbers smaller than about 2) remains practically constant (unaffected by the flow). As the Wi number is increased above approximately 2, the average number of entanglements per chain starts to decrease significantly with the applied flow; this is a direct manifestation of the strong alignment of chains with the flow at these high shear rates. The physical picture that emerges here is that of an ensemble of chains which are significantly oriented along the flow to a degree that they can slide past each other and thus get disentangled compared to the equilibrium case. Chain disentanglement is supposed to be accompanied by a reduction in the viscosity of the melt, so at a given shear rate it is of interest to examine the relationship between the computed average number of entanglement points per chain $\langle Z_{es} \rangle$ and the predicted value of the shear viscosity at the same shear rate. To reveal the intimate interrelationship between melt viscosity η and average number of entanglements per chain $\langle Z_{es} \rangle$, we present a log−log plot of $\langle Z_{es} \rangle$ vs Wi in the inset of Figure 13b which indeed shows a close resemblance with Figure 4a for the viscosity function.

An important point to make about the simulation data shown in Figure 13b is the following: According to experimental data for M_e (as estimated based on the plateau modulus using $G_N^0 = (4/5) \rho RT/M_e$),[87] the average number of entanglement points in the $C_{400}H_{802}$ linear PE melt at $T = 450$ K and density $\rho = 0.7640$ g/cm^3 should be approximately equal to 6. The corresponding value from our direct topological analysis is $\langle Z_{es} \rangle = 11.5 \pm 0.8$, i.e., almost twice as large. This point has also been discussed by Foteinopoulou et al.,[61] Tzoumanekas-Theodorou,[58] and Masubuchi et al.[98] and is usually attributed to the many assumptions behind the formula $G_N^0 = (4/5)\rho RT/M_e$, such as a Gaussian-type (i.e., purely entropic) spring force law for the response of the corresponding network of PPs to a deformation, affine transformation of polymer chains under flow, Rouse-type relaxation of chain topology and entanglement, and many others.

End-To-End Length and Number of Monomers of an Entanglement Strand. The end-to-end length of an entanglement strand is an important measure of the spacing between entanglements. In Figure 14a, we show plots of the probability distribution function $P(d_{es})$ of the length of an entanglement strand as a function of the applied flow. At equilibrium and in accordance with analytical theories[97] and a coarse-grained primitive chain network model,[99] $P(d_{es})$ follows a Poisson distribution. Our NEMD data show that $P(d_{es})$ remains Poisson-like also at low shear rates (corresponding to Wi numbers approximately smaller than 1). At higher shear rates, the distribution broadens up and the position of its peak shifts slightly to smaller d_{es} values, which should be contrasted with the behavior of the distribution functions for L_{pp} and Z_{es} shown in Figures 12a and 13a, respectively. It is indicative again of an overall collapsed configuration for the mesoscopic shape of the chain under a strong shear flow due to fast rotation and tumbling. We also note that although the overall curves at high shear rates have shapes that apparently resemble a Poisson distribution, they are quantitatively very different from the true Poisson curve based on the same mean value.
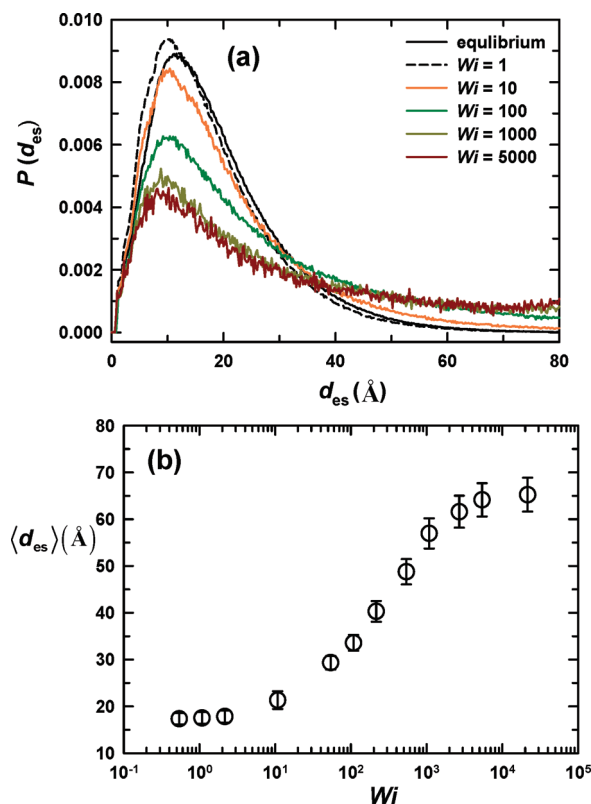
Figure 14. Same as with Figure 12, but for the end-to-end length d_{es} of an entanglement strand.

In Figure 14b we present how the flow affects the average length $\langle d_{es}\rangle$ of an entanglement strand. For low enough shear rates corresponding to Wi numbers smaller than about 3, $\langle d_{es}\rangle$ remains practically unaffected by the flow. For flows corresponding to Wi numbers larger than about 3, on the other hand, $\langle d_{es}\rangle$ increases rapidly with shear rate, it reaches an asymptotic value equal to ~65 Å for a Wi number approximately equal to 10000 and then remains practically constant. The plateau value is by a factor of 3.5 larger than the equilibrium value. Although the NEMD results for the behavior of $\langle d_{es}\rangle$ with the applied shear flow should be analyzed in conjunction with the corresponding results for the contour length L_{pp} of the PPs (shown in Figure 12b), they reveal again the significant reduction in the degree of topological interaction between chains at the highest shear fields and are fully consistent with the corresponding results for the dependence of the average number of entanglement strands per chain $\langle Z_{es}\rangle$ on shear rate (shown in Figure 13b). It is also noted that the nonmonotonic behavior of L_{pp} (Figure 12b) can be understood by considering the combined effect of the entanglement strand distance d_{es} (Figure 14b) and the number of entanglement strands Z_{es} (Figure 13b). That is, while the average value of d_{es} increases with the shear rate, the corresponding value of Z_{es} decreases.

The corresponding NEMD results for the effect of flow on the probability distribution function $P(N_{es})$ and the average number $\langle N_{es}\rangle$ of the number of carbon atoms in an entanglement strand are shown in parts a and b of Figure 15, respectively. As should have been expected, the curves obtained are very similar to those for the (end-to-end) length d_{es} of an entanglement strand (e.g., the asymptotic value of $\langle N_{es}\rangle$ at high flow fields is approximately three times larger than its equilibrium value). We also note that qualitatively similar behaviors have been observed in previous equilibrium atomistic Monte Carlo[58,61] and coarse-grained equilibrium[99,100] and nonequilibrium[101] simulations.
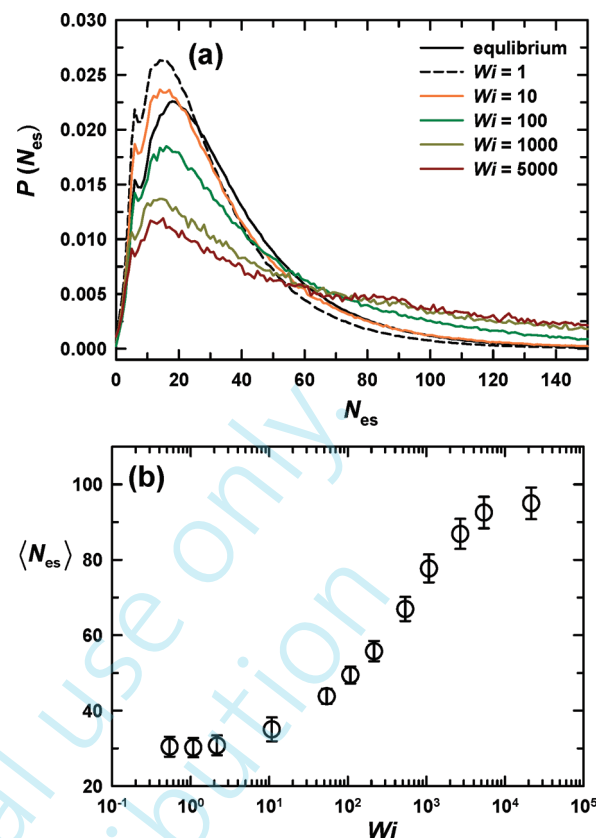

Figure 15. Same as with Figure 12, but for the number N_{es} of carbon atoms per entanglement strand.

Indirect Topological Measures Considering PPs as Random Walks. If PPs are assumed to obey Gaussian statistics and entanglement strands are identified with the PP Kuhn segment, then one can make use of the following relationships of the tube theory

$$d_{pp} = \frac{\langle R^2\rangle}{\langle L_{pp}\rangle}; \quad Z_{pp} = \frac{\langle L_{pp}\rangle^2}{\langle R^2\rangle}; \quad N_{pp} = N\frac{\langle R^2\rangle}{\langle L_{pp}\rangle^2} \quad (11)$$

to obtain the tube diameter d_{pp}, the number Z_{pp} of PP Kuhn segments, and the number N_{pp} of carbon atoms per PP Kuhn segment using the values of $\langle L_{pp}\rangle$ and $\langle R^2\rangle$ obtained directly from the PP analysis with the Z1 algorithm. The corresponding results are reported in Figure 16. For example, the variation of d_{pp} with the Wi number is shown in Figure 16a. Although qualitatively the results are similar to those for the variation of the length of an entanglement strands d_{es} with the Wi number obtained directly from the PP analysis, quantitatively one can observe a number of differences: (a) The value of d_{pp} at equilibrium is 37 ± 1 Å, that is almost twice the corresponding value of d_{es} (~18.9 Å); this value (37 ± 1 Å) is consistent with the value obtained with the CReTA algorithm[58] ($d_{pp} \approx 38$ Å) and the one reported experimentally ($d_{pp} \approx 40$ Å).[58,102,103] (b) The ratio of the asymptotic value of d_{pp} at high shear rates to that at equilibrium is approximately 6 times; this is considerably larger than the corresponding value (~3.5) based on d_{es}. The discrepancy should be attributed to the non-Gaussian character of the PPs at high shear rates, implying that eq 11 is no longer valid under strong flow fields. Similar conclusions can be drawn by analyzing the results for Z_{pp} and N_{pp}, shown in Figure 16b and 16c, respectively. A point to note here is that the values $Z_{pp} \approx 6$ and $N_{pp} \approx 65$ at equilibrium are in favorable agreement with the corresponding experimental values of $Z_{pp} \approx 6$ and $N_{pp} \approx 68$ reported by Fetters et al.[87]
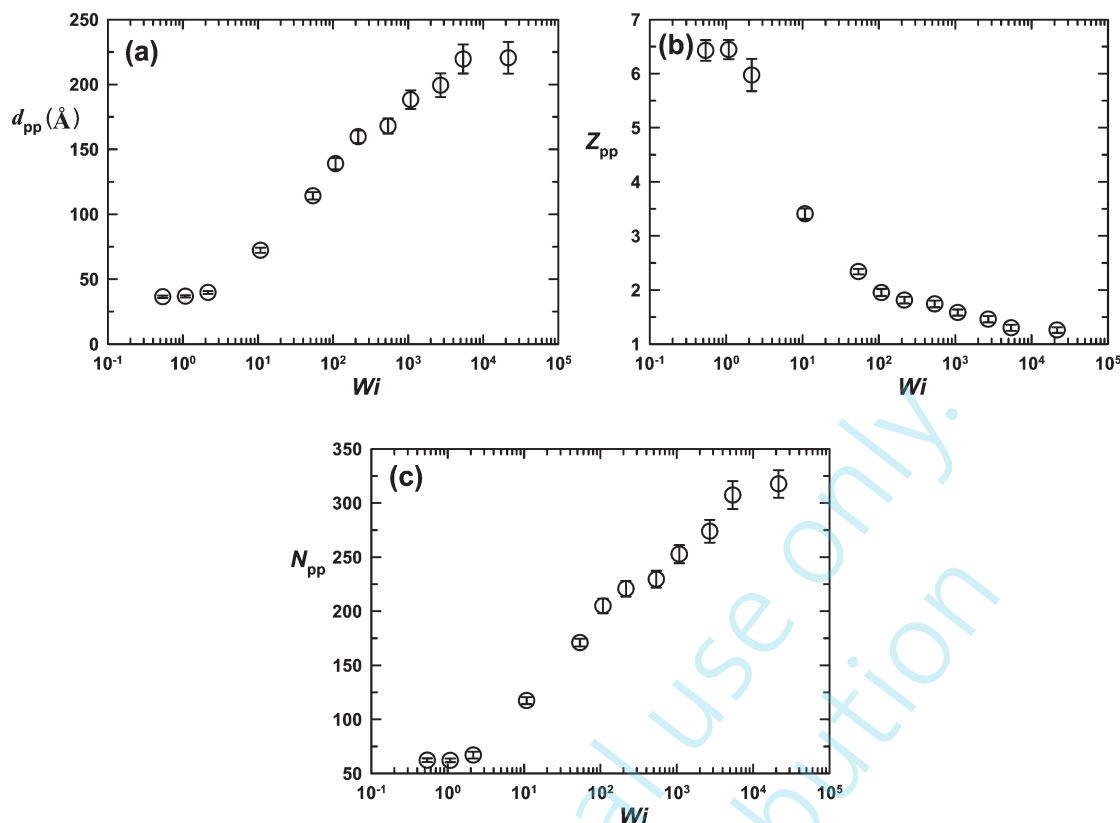
Figure 16. Variation of (a) the tube diameter d_{pp}, (b) the number Z_{pp} of PP Kuhn segments, and (c) the number N_{pp} of carbon atoms in a PP Kuhn segment with shear rate, as computed with the help of eq 11 by making use of the $\langle L_{pp} \rangle$ and $\langle R^2 \rangle$ data obtained directly from the PP analysis with the Z1 algorithm.

Overall, we can say that the results obtained indirectly for the variation of the tube diameter d_{pp}, the number Z_{pp} of PP Kuhn segments, and the number N_{pp} of carbon atoms per PP Kuhn segment on the basis of eq 11 are qualitatively consistent with those computed directly from the PP analysis; however, significant quantitative differences are observed between the two sets which become more pronounced at the highest shear rates due to the Gaussian assumption behind eq 11 for the PP Kuhn length which breaks down at high flow fields.

4. Conclusions and Outlook

Molecular-level information is absolutely necessary for developing robust and sound multiscale modeling procedures for predicting the macroscopic transient and steady state processing behavior of polymeric materials. The approach must have the necessary mathematical and physical depth at each time and length scale level to fully describe important parameters which should be generated through specific algorithms linking the micro, meso, and macro levels. Presently, nonequilibrium viscoelastic processing flows cannot be easily characterized (or even formulated) within one macroscopic model. The reason relates to the myriad of relaxation phenomena occurring at multiple length and time scales within these materials. To evaluate, in particular, constitutive equations for multiple polymer architectures or to develop models that incorporate convective constraint release for fast polymeric flows requires input from atomistic simulations for the interplay between applied flow and system structure at various levels. To this, direct NEMD simulations based on rigorous algorithms formulated on principles of nonequilibrium statistical mechanics together with accurate potential functions describing the interactions between atomistic units are considered today as a very useful tool capable of providing invaluable microscopic information for a variety of effects referring to the

response of a polymeric liquid to an applied flow field. In the present work, we have exploited NEMD simulations in order to understand how a shear flow affects the overall chain conformation of a moderately entangled linear PE melt, how it alters the entanglement network underlying topology in this melt due to chain continuity and chain uncrossability, the relationship between stress tensor and birefringence tensor, and many others. We consider therefore this work as just the first step toward a more comprehensive understanding of the interaction of a polymer melt with a flow, a very complicated problem including among others poorly understood components today, such as what is the role of molecular architecture, how the type of flow (shear versus elongation) affects the system topology, etc.

Beyond the linear flow regime (e.g., $Wi > 2$), a variety of structural, rheological and topological properties are found to display significant deviations from their corresponding equilibrium behaviors; e.g., (a) non-Gaussian shape of the distribution function $P(|\mathbf{R}|)$ of the magnitude $|\mathbf{R}|$ of the chain end-to-end vector, (b) increase of the ratio $\langle R^2 \rangle / \langle R_g{}^2 \rangle$ (radius of gyration R_g) above its equilibrium value (≈ 6), (c) shear-thinning behavior of viscosity and normal stress coefficients, (d) breakdown of the stress-optical rule, (e) distortion of intrinsic molecular shape, and many others.

Particularly noticeable features are observed in shear flow such as (i) asymptotic behavior of $\langle R^2 \rangle$ at very high shear rates which is only $\sim 25\%$ of the maximum possible value, (ii) two peaks (one at small and one at large $|\mathbf{R}|$ values) in $P(|\mathbf{R}|)$ at high shear rates, (iii) maximum behavior exhibited by $\tilde{c}_{xy}$ at intermediate flow strength, (iv) maximum and minimum behavior displayed in the intramolecular- and intermolecular Lennard-Jones energy plots, respectively, (v) plateau (or minimum) in hydrostatic pressure at high shear rates, (vi) intrinsic molecular shape of the chains becoming fatter in the middle part and sharper near the end

points of their cloud distribution (thus leading to more uniform segment distribution along the chain) with increasing shear field, (vii) maximum behavior of the average PP contour length at intermediate shear rate, and (viii) *shear-thinning* behavior of the average number of entanglements per chain. All these complicated phenomena can be adequately explained by considering the combined effects of chain orientation/stretching and chain rotation/tumbling. It is also noted that many of these features (except those of topological measures) observed in the present entangled PE melt under shear flow bear qualitative similarities to those reported in the literature from NEMD simulations with short, unentangled polymer melts under shear.[12,38,50,80,90] However, the absolute magnitude of the flow effects on each of these phenomena is generally expected to be much more distinctive in the case of entangled polymers, as supported by previous works[12,30,31,38] Besides, the detailed molecular mechanisms underlying the rheological behaviors can be very different between unentangled and entangled polymers, due to the absence and presence of topological constraints between chains in the former and latter case, respectively. We also note that most features exhibited by topological measures (the PP contour length, the number of entanglements, and entanglement strand characteristics) due to shear are expected to be common to other types of polymer (not only linear but also branched polymers) as well, irrespective of the molecular weight and the entanglement molecular weight.

In the present work, we have restricted our analysis only to the average (static-like) properties of the entanglement network underlying topology in an entangled polymer melt. From the rheological point of view, chain dynamics at the level of Ps has been one of the most important and challenging subjects in the field. How to map, for example, atomistic trajectories onto trajectories of PPs has been addressed only very recently by Stephanou et al.[104] who proposed a novel methodology for interfacing the results of atomistic MD simulations with the tube model. By combining this very promising methodology with the results of the present NEMD simulations will allow us to address in a future study issues related with the dynamics of PPs under flow conditions. Among other things, this would help us gain a deeper understanding of some important mechanisms typically assumed in modern tube models such as convective constraint release (CCR),[105,106] directly from atomistic (lower-level) simulations.

Note Added after ASAP Publication. This paper was published on the Web on July 15, 2010, with two minor errors in the caption for Figure 7. The corrected version was reposted on July 21, 2010.

Supporting Information Available: Text giving time integrators for the phase-space variables with the *r*-RESPA of the *p*-SLLOD equations of motion implemented with a Nosé–Hoover thermostat (eq 5) for simple shear flow and planar elongational flow. This material is available free of charge via the Internet at http://pubs.acs.org.

References and Notes

(1) Ferry, J. D. *Viscoelastic Properties of Polymers*, 3rd ed.; John Wiley & Sons: New York, 1980.
(2) Bird, R. B.; Armstrong, R. C.; Hassager, O. *Dynamics of Polymeric Liquids, Fluid Mechanics*, 2nd ed.; Wiley-Interscience: New York, 1987; Vol. *1*.
(3) Larson, R. G. *The Structure and Rheology of Complex Fluids*; Oxford University Press: New York, 1999.
(4) McLeish, T. C. B. *Adv. Phys.* **2002**, *51*, 1379.
(5) Flory, P. J. *Statistical Mechanics of Chain Molecules*; Wiley-Interscience: New York, 1969.
(6) de Gennes, P. G. *Scaling Concepts in Polymer Physics*; Cornell University Press: Ithaca, NY, 1979.
(7) Doi, M.; Edwards, S. F. *The Theory of Polymer Dynamics*; Clarendon Press: New York, 1986.
(8) Beris, A. N.; Edwards, B. J. *Thermodynamics of Flowing Systems with Internal Microstructure*; Oxford University Press: New York, 1994.
(9) Meissner, J. *Pure. Appl. Chem.* **1975**, *42*, 551.
(10) Laun, H. M.; Schuch, H. *J. Rheol.* **1989**, *33*, 119.
(11) Bach, A.; Rasmussen, H. K.; Hassager, O. *J. Rheol.* **2003**, *47*, 429.
(12) Baig, C.; Mavrantzas, V. G. *J. Chem. Phys.* **2010**, *132*, 014904.
(13) Maier, B.; Bensimon, D.; Croquette, V. *Proc. Natl. Acad. Sci. U.S.A.* **2000**, *97*, 12002.
(14) Goel, A.; Frank-Kamenetskii, M. D.; Ellenberger, T.; Herschbach, D. *Proc. Natl. Acad. Sci. U.S.A.* **2001**, *98*, 8485.
(15) Doufas, A. K.; Dairenieh, I. S.; McHugh, A. J. *J. Rheol.* **1999**, *43*, 85.
(16) Dukovski, I.; Muthukumar, M. *J. Chem. Phys.* **2003**, *118*, 6648.
(17) Lavine, M. S.; Waheed, N.; Rutledge, G. C. *Polymer* **2003**, *44*, 1771.
(18) Somani, R. H.; Yang, L.; Zhu, L.; Hsiao, B. S. *Polymer* **2005**, *46*, 8587.
(19) Ionescu, T. C.; Baig, C.; Edwards, B. J.; Keffer, D. J.; Habenschuss, A. *Phys. Rev. Lett.* **2006**, *96*, 037802.
(20) Kimata, S.; Sakurai, T.; Nozue, Y.; Kasahara, T.; Yamaguchi, N.; Karino, T.; Shibayama, M.; Kornfield, J. *Science* **2007**, *316*, 1014.
(21) Zhao, B.; Li, X.; Huang, Y.; Cong, Y.; Ma, Z.; Shao, C.; An, H.; Yan, T.; Li, L. *Macromolecules* **2009**, *42*, 1428.
(22) Baig, C.; Edwards, B. J. *Europhys. Lett.* **2010**, *89*, 36003.
(23) Balzano, L.; Kukalyekar, N.; Rastogi, S.; Peters, G. W. M.; Chadwick, J. C. *Phys. Rev. Lett.* **2008**, *100*, 048302.
(24) Tskhovrebova, L.; Trinick, J.; Sleep, J. A.; Simmons, R. M. *Nature* **1997**, *387*, 308.
(25) Smith, D. E.; Babcock, H. P.; Chu, S. *Science* **1999**, *283*, 1724.
(26) Robertson, R. M.; Smith, D. E. *Proc. Natl. Acad. Sci. U.S.A.* **2007**, *104*, 4824.
(27) Evans, D. J.; Morriss, G. P. *Statistical Mechanics of Nonequilibrium Liquids*; Academic Press: New York, 1990.
(28) Baig, C.; Edwards, B. J.; Keffer, D. J.; Cochran, H. D. *J. Chem. Phys.* **2005**, *122*, 114103.
(29) Edwards, B. J.; Baig, C.; Keffer, D. J. *J. Chem. Phys.* **2005**, *123*, 114106.
(30) Baig, C.; Edwards, B. J.; Keffer, D. J.; Cochran, H. D. *J. Chem. Phys.* **2005**, *122*, 184906.
(31) Baig, C.; Edwards, B. J.; Keffer, D. J.; Cochran, H. D.; Harmandaris, V. A. *J. Chem. Phys.* **2006**, *124*, 084902.
(32) Moore, J. D.; Cui, S. T.; Cochran, H. D.; Cummings, P. T. *J. Non-Newtonian Fluid Mech.* **2000**, *93*, 83.
(33) Lees, A. W.; Edwards, S. F. *J. Phys. C* **1972**, *5*, 1921.
(34) Kraynik, A. M.; Reinelt, D. A. *Int. J. Multiphase Flow* **1992**, *18*, 1045.
(35) Todd, B. D.; Daivis, P. J. *Phys. Rev. Lett.* **1998**, *81*, 1118. *Comput. Phys. Commun.* **1999**, *117*, 191.
(36) Ilg, P.; Öttinger, H. C.; Kröger, M. *Phys. Rev. E* **2009**, *79*, 011802.
(37) Kröger, M. *Models for polymeric and anisotropic liquids*; Springer: New York, 2005.
(38) Kim, J. M.; Keffer, D. J.; Kröger, M.; Edwards, B. J. *J. Non-Newtonian Fluid Mech.* **2008**, *152*, 168.
(39) Allen, M. P.; Tildesley, D. J. *Computer Simulation of Liquids*; Clarendon Press: Oxford, 1987.
(40) Kröger, M.; Loose, W.; Hess, S. *J. Rheol.* **1993**, *37*, 1057.
(41) Kröger, M. *Appl. Rheol.* **1995**, *5*, 66.
(42) Kröger, M.; Hess, S. *Phys. Rev. Lett.* **2000**, *85*, 1128.
(43) Doi, M.; Aoyagi, T. *Comput. Theor. Polym. Sci.* **2000**, *10*, 317.
(44) Kröger, M.; Luap, C.; Müller, R. *Macromolecules* **1997**, *30*, 526.
(45) Daivis, P. J.; Matin, M. L.; Todd, B. D. *J. Non-Newtonian Fluid Mech.* **2003**, *111*, 1.
(46) Kröger, M. *Phys. Rep.* **2004**, *390*, 453.
(47) Todd, B. D.; Hunt, T. A. *J. Chem. Phys.* **2009**, *131*, 054904.
(48) Le, T. C.; Todd, B. D.; Daivis, P. J.; Uhlherr, A. *J. Chem. Phys.* **2009**, *131*, 044902.
(49) Padding, J. T.; Briels, W. J. *J. Chem. Phys.* **2003**, *118*, 10276.

(50) Baig, C.; Harmandaris, V. A. *Macromolecules* **2010**, *43*, 3156.
(51) de Gennes, P. G. *J. Chem. Phys.* **1971**, *55*, 572.
(52) Doi, M.; Edwards, S. F. *J. Chem. Soc. Faraday Trans.* **1978**, *74*, 1789. Doi, M.; Edwards, S. F. *J. Chem. Soc. Faraday Trans.* **1978**, *74*, 1802. Doi, M.; Edwards, S. F. *J. Chem. Soc. Faraday Trans.* **1978**, *74*, 1818. Doi, M.; Edwards, S. F. *J. Chem. Soc. Faraday Trans.* **1979**, *75*, 38.
(53) Edwards, S. F. *Br. Polym. J.* **1977**, *9*, 140.
(54) Everaers, R.; Sukumaran, S. K.; Grest, G. S.; Svaneborg, C.; Sivasubramanian, A.; Kremer, K. *Science* **2004**, *303*, 823.
(55) Rubinstein, M.; Helfand, E. *J. Chem. Phys.* **1985**, *82*, 2477.
(56) Sukumaran, S. K.; Grest, G. S.; Kremer, K.; Everaers, R. *J. Polym. Sci., Polym. Phys. Ed.* **2005**, *43*, 917.
(57) Kröger, M. *Comput. Phys. Commun.* **2005**, *168*, 209. Kröger, M.; Ramirez, J.; Öttinger, H. C. *Polymer* **2002**, *43*, 477.
(58) Tzoumanekas, C.; Theodorou, D. N. *Macromolecules* **2006**, *39*, 4592.
(59) Shanbhag, S.; Kröger, M. *Macromolecules* **2007**, *40*, 2897.
(60) Z1 code online for testing at http://www.complexfluids.ethz.ch/cgi-bin/Z1.
(61) Foteinopoulou, K.; Karayiannis, N. C.; Mavrantzas, V. G.; Kröger, M. *Macromolecules* **2006**, *39*, 4207.
(62) Karayiannis, N. C.; Kröger, M. *Int. J. Mol. Sci.* **2009**, *10*, 5054.
(63) Karayiannis, N. C.; Mavrantzas, V. G.; Theodorou, D. N. *Phys. Rev. Lett.* **2002**, *88*, 105503.
(64) Dee, G. T.; Ougizawa, T.; Walsh, D. J. *Polymer* **1992**, *33*, 3462.
(65) Siepmann, J. I.; Karaborni, S.; Smit, B. *Nature* **1993**, *365*, 330.
(66) Nose, S. *Mol. Phys.* **1984**, *52*, 255. *J. Chem. Phys.* **1984**, *81*, 511.
(67) Hoover, W. G. *Phys. Rev. A* **1985**, *31*, 1695.
(68) Tuckerman, M.; Berne, B. J.; Martyna, G. J. *J. Chem. Phys.* **1992**, *97*, 1990.
(69) Tzoumanekas, C.; Theodorou, D. N. *Curr. Opin. Solid State Mater. Sci.* **2006**, *10*, 61.
(70) Tzoumanekas, C.; Lahmar, F.; Rousseau, B.; Theodorou, D. N. *Macromolecules* **2009**, *42*, 7474.
(71) Lahmar, F.; Tzoumanekas, C.; Theodorou, D. N.; Rousseau, B. *Macromolecules* **2009**, *42*, 7485.
(72) Kim, J. M.; Edwards, B. J.; Keffer, D. J.; Khomami, B. *Phys. Lett. A* **2009**, *373*, 769.
(73) Baig, C.; Mavrantzas, V. G. *Phys. Rev. B* **2009**, *79*, 144302.
(74) Smith, D. E.; Babcock, H. P.; Chu, S. *Science* **1999**, *283*, 1724.
(75) Teixeira, R. E.; Dambal, A. K.; Richter, D. H.; Shaqfeh, E. S. G.; Chu, S. *Macromolecules* **2007**, *40*, 2461.
(76) Aust, C.; Kröger, M.; Hess, S. *Macromolecules* **2002**, *35*, 8621.
(77) de Gennes, P. G. *Science* **1997**, *276*, 1999.
(78) Gorban, A. N.; Karlin, I. V. *Physica A* **2004**, *336*, 391.
(79) Bird, R. B.; Armstrong, R. C.; Hassager, O. *Dynamics of Polymeric Liquids, Kinetic Theory*, 2nd ed.; Wiley-Interscience: New York, 1987; Vol. 2.
(80) Baig, C.; Jiang, B.; Edwards, B. J.; Keffer, D. J.; Cochran, H. D. *J. Rheol.* **2006**, *50*, 625.
(81) Stephanou, P. S.; Baig, C.; Mavrantzas, V. G. *J. Rheol.* **2009**, *53*, 309.
(82) Fang, J.; Kröger, M.; Öttinger, H. C. *J. Rheol.* **2000**, *44*, 1293.
(83) Schieber, J. D.; Neergaard, J.; Gupta, S. *J. Rheol.* **2003**, *47*, 213.
(84) Padding, J. T.; Briels, W. J. *J. Chem. Phys.* **2002**, *117*, 925.
(85) Baig, C.; Mavrantzas, V. G. *Phys. Rev. Lett.* **2007**, *99*, 257801.
(86) Irving, J. H.; Kirkwood, J. G. *J. Chem. Phys.* **1950**, *18*, 817.
(87) Fetters, L. J.; Lohse, D. J.; Milner, S. T.; Graessley, W. W. *Macromolecules* **1999**, *32*, 6847.
(88) Khare, R.; de Pablo, J.; Yethiraj, A. *J. Chem. Phys.* **1997**, *107*, 6956.
(89) Mavrantzas, V. G.; Theodorou, D. N. *Comput. Theor. Polymer Sci.* **2000**, *10*, 1.
(90) Baig, C.; Edwards, B. J.; Keffer, D. J. *Rheol. Acta* **2007**, *46*, 1171.
(91) Luap, C.; Müller, C.; Schweizer, T.; Venerus, D. C. *Rheol. Acta* **2005**, *45*, 83.
(92) Janeschitz-Kriegl, H. *Polymer melt rheology and flow birefringence*; Springer-Verlag: New York, 1983.
(93) Baig, C.; Kalyuzhnyi, Yu. V.; Cui, S. T.; Cochran, H. D. *Phys. Rev. E* **2004**, *70*, 061204.
(94) The isosurface plots shown in Figure 6 of ref 12 were made based on the relative monomer density compared to the maximum monomer density in the segment cloud, whereas the plots presented in Figure 10 in this study have been made based on the percentage of the total number of monomers in the chain. Although both descriptions are equally capable of representing the general feature of segmental distribution of chain, it seems that the present approach based on the percentage of the total number of monomers is more representative of intrinsic molecular shape than that employed in ref 12, since the maximum segmental density may be largely fluctuating (statistically less accurate) depending on the system conditions and also may exhibit an abnormally large (or small) value for some irregular systems.
(95) Šolc, K.; Stockmayer, W. H. *J. Chem. Phys.* **1971**, *54*, 2756.
(96) Theodorou, D. N.; Suter, U. W. *Macromolecules* **1985**, *18*, 1206.
(97) Schieber, J. D. *J. Chem. Phys.* **2003**, *118*, 5162.
(98) Masubuchi, Y.; Ianniruberto, G.; Greco, F.; Marrucci, G. *J. Chem. Phys.* **2003**, *119*, 6925.
(99) Masubuchi, Y.; Uneyama, T.; Watanabe, H.; Ianniruberto, G.; Greco, F.; Marrucci, G. *J. Chem. Phys.* **2010**, *132*, 134902.
(100) Shanbhag, S.; Larson, R. G. *Macromolecules* **2006**, *39*, 2413.
(101) Masubuchi, Y.; Furuichi, K.; Horio, K.; Uneyama, T.; Watanabe, H.; Ianniruberto, G.; Greco, F.; Marrucci, G. *J. Chem. Phys.* **2009**, *131*, 114906.
(102) Fetters, L. J.; Lohse, D. J.; Richter, D.; Witten, T. A.; Zirkel, A. *Macromolecules* **1994**, *27*, 4639.
(103) Fetters, L. J.; Lohse, D. J.; Graessley, W. W. *J. Polym. Sci., Part B: Polym. Phys.* **1999**, *37*, 1023.
(104) Stephanou, P. S.; Baig, C.; Tsolou, G.; Mavrantzas, V. G.; Kröger, M. *J. Chem. Phys.* **2010**, *132*, 124904.
(105) Marrucci, G. *J. Non-Newtonian Fluid Mech.* **1996**, *62*, 279.
(106) Ianniruberto, G.; Marrucci, G. *J. Non-Newtonian Fluid Mech.* **1996**, *65*, 24.